REVISION 1- re-submitted to *American Mineralogist*

Synthesis and characterization of Fe(III)-Fe(II)- Mg- Al smectite solid solutions and implications for planetary science

Valerie K. Fox[1*], Robert J. Kupper[2], Bethany L. Ehlmann[1,3], Jeffrey G. Catalano[2], Joseph Razzell-Hollis[3], William J. Abbey[3], Dirk J. Schild[1], Ryan D. Nickerson[2], Jonas C. Peters[1], Sydney M Katz[2†], Andrew A. White[2]

[1] California Institute of Technology, 1200 E California Blvd, Pasadena, CA, 91125

[2] Washington University in St. Louis, 1 Brookings Drive, CB 1169, St. Louis, MO, 63130

[3] NASA Jet Propulsion Laboratory, 4800 Oak Grove Dr, Pasadena, CA 91109

*Present Address: University of Minnesota, John T. Tate Hall, 116 Church Street SE, Minneapolis, MN 55455-0149. USA

† Present Address: Department of Aeronautic and Astronautics, Stanford University, Stanford, CA 94305, USA

Key Words: Smectites, Clay Mineralogy, Reflectance spectroscopy, XRD, Raman spectra, Mars, Planetary Science

Abstract

This study demonstrates the synergies and limits of multiple measurement types for the detection of smectite chemistry and oxidation state on planetary surfaces to infer past geochemical conditions. Smectite clay minerals are common products of water-rock interactions throughout the solar system, and their detection and characterization provides important clues about geochemical conditions and past environments if sufficient information about their composition can be discerned. Here, we synthesize and report on the spectroscopic properties of a suite of smectite samples that span the intermediate compositional range between Fe(II,), Fe(III), Mg, and Al end-member species using bulk chemical analyses, x-ray diffraction, Vis/IR reflectance spectroscopy, UV and green-laser Raman spectroscopy, and Mössbauer spectroscopy. Our data show that smectite composition and the oxidation state of octahedral Fe can be reliably identified in the near infrared on the basis of combination and fundamental metal-OH stretching modes between 2.1-2.9μm, which vary systematically with chemistry. Smectites dominated by Mg or Fe(III) have spectrally distinct fundamental and combinations stretches, whereas Al-rich and Fe(II) rich smectites have similar fundamental minima near 2.76μm, but have distinct combination M-OH features between 2.24 and 2.36μm. We show that with expanded spectral libraries that include intermediate composition smectites and both Fe(III) and Fe(II) oxidation states, more refined characterization of smectites from MIR data is now possible, as the position of the 450cm^{-1} absorption shifts systematically with octahedral Fe content, although detailed analysis is best accomplished in concert with other characterization methods. Our data also

provides the first Raman spectral libraries of smectite clays as a function of chemistry, and we demonstrate that Raman spectroscopy at multiple excitation wavelengths, can qualitatively distinguish smectite clays of different structures, and can enhance interpretation by other types of analyses. Our sample set demonstrates how X-ray diffraction can distinguish between dioctahedral and trioctahedral smectites using either the (02,11) or (06,33) peaks, but auxiliary information about chemistry and oxidation state aids in specific identifications. Finally, the temperature-dependent isomer shift and quadrupole splitting in Mössbauer data are insensitive to changes in Fe content but reliability differentiate Fe within the smectite mineral structure.

1. Introduction

Smectite clay minerals are among the most common products of water-rock interactions detected throughout the solar system and are key indicators of the geochemistry, oxidation state, and extent of aqueous activity in the environment in which they formed (Gates 2005; Bishop et al. 2008a; Ehlmann et al. 2011; Catalano, 2013, Michalski et al. 2015; Gainey et al. 2017, Bristow et al. 2018). Tracing the history of aqueous alteration is a crucial aspect of understanding the formation and evolution of planetary bodies and water reservoirs throughout the solar system. Smectites are 2:1 layer phyllosilicates, comprised of an octahedral sheet between two Si(Al)-O tetrahedral sheets with an expandable interlayer, which contains H_2O and exchangeable cations that balance charge of the overall structure. A generalized

formula is $(Ca,Na)_{0.3-0.5}(Fe,Mg,Al)_{2-3}(Si,Al)_4O_{10}(OH)_2 \bullet nH_2O$. Occupancy of the octahedral sheet is used to classify smectite minerals: trioctahedral smectites have all octahedral sites filled and are dominated by +2 cations; dioctahedral smectites have two of three octahedral sites filled and are dominated by +3 cations. There are a number of major endmember species, including dioctahedral nontronites (Fe(III)-rich), montmorillonites and beidellites (Al-rich), and trioctahedral saponites (Mg or Fe(II)-rich).

On Mars, smectite-bearing outcrops have been detected on the surface by orbital infrared instruments (Poulet et al. 2005; Bibring et al. 2006; Bishop et al. 2008a; Poulet et al. 2008; Ehlmann et al. 2011; Carter et al. 2013, Ehlmann and Edwards 2014), and have also been investigated in-situ by both the MER Opportunity rover (Arvidson et al. 2014; Fox et al. 2016) and the Mars Science Laboratory (MSL) Curiosity rover (Vaniman et al. 2013; Grotzinger et al. 2014; Bristow et al. 2015, 2018; Rampe et al. 2017). Fe and Mg-bearing smectites are the most common phyllosilicates detected on Mars, and are found in most exposures of ancient crust, suggesting early conditions conducive to silicate weathering or hydrothermal alteration (Poulet et al. 2005; Bishop et al. 2008a; Ehlmann et al. 2011; Carter et al. 2013; Catalano 2013; Ehlmann and Edwards 2014; Michalski et al. 2015). Fe- and Mg-bearing phyllosilicates, including smectites, are also found in carbonaceous chondrite meteorites and detected on other altered solar system bodies such as Ceres, C-class asteroids, and comets (Bunch and Chang 1980; Rivkin et al. 2003, 2006; De Sanctis et al. 2015; Ammannito et al. 2016). Due to their ubiquity and

94 geochemical sensitivity to their formation environment, Fe- and Mg-bearing
95 smectites are a key target material in planetary exploration in seeking to
96 understand the aqueous history of the solar system. Their composition, along with
97 Fe oxidation state, can be indicative of the aqueous conditions that altered the host
98 material to the clay, if the properties can be discerned.
99
100 A wide range of smectites are observed on Earth with aluminous smectites
101 (montmorillonite, beidellite) found most extensively in continental settings because
102 of alteration of the predominantly felsic continental crust (Figure 1). Nontronites
103 and a wide range of intermediate Fe/Mg smectites are observed in oceanic settings
104 and continental settings with basaltic rocks. Smectites formed in subsurface settings
105 contain substantial ferrous (Fe(II)) iron rather than the typical ferric (Fe(III))
106 smectites that form in soils, terrestrial sediments, and on the ocean floor where
107 dissolved O_2 is abundant. The crusts of planetary bodies are generally dominated by
108 rocks of mafic and ultramafic compositions, and most non-terrestrial bodies also
109 lack an oxidizing atmosphere. Indeed, some have postulated the early Martian
110 atmosphere was anoxic and there is widespread evidence for Earth's anoxic early
111 atmosphere (Catling and Moore 2003; Catalano 2013; Sholes et al. 2017).
112 Consequently, Fe/Mg smectites of intermediate composition, containing Fe(II),
113 Fe(III), or mixtures of the two, are expected to be common products forming on
114 such bodies (Guven 1988; Burns 1993).
115

A few well-characterized smectite samples from terrestrial deposits, particularly from the Clay Mineral Society Special Clays, have found widespread use as spectral standards for identifying mineral phases on planetary bodies (Michalski et al. 2006; Bishop et al. 2008b; Treiman et al. 2014). The Al smectites (montmorillonites, beidellites) and endmember Fe(III) smectites (nontronites) are well-represented; a relatively limited compositional range of Mg smectites is represented by one common saponite standard. However, there is a large compositional range, representing Fe- and Mg-rich di- and trioctahedral smectites that form from terrestrial alteration, for which there are no common standards (Figure 1). In addition, while Fe(III)-bearing smectites (nontronites and also montmorillonites with moderate Fe contents) are well characterized, smectites containing Fe(II) or mixtures of Fe(II) and Fe(III) are poorly described because they are unstable against oxidation in air(Kohyama et al. 1973; Badaut et al. 1985; Guven 1988; Lajarige et al. 1998).

There has been significant effort to characterize the structural behavior as composition varies along binary axes by synthesizing smectites with controlled compositions and octahedral cation proportions. The Fe(III)-Mg (nontronite-saponite) series is a true solid solution in the absence of Al (Grauby et al. 1994), as is the Fe(III)-Al (nontronite-beidellite) series (Petit et al. 2015). The Al-Mg series (beidellite-saponite) is found to have an immiscibility gap that averages out in bulk measurements due to variability in the molecular structure within a clay particle (Grauby et al. 1993). There have been limited studies of native Fe(II)-bearing

smectites, primarily trioctahedral in nature, and the impacts of oxidation on their structures (Chemtob et al. 2015; Chemtob et al. 2017). The substantial body of work on chemically reduced dioctahedral smectites that originally contained Fe(III) are instructive but of uncertain value to the present work, as such transformations result in dihydroxylation, perturbed layer charge, and rearrangement of octahedral cations (Manceau et al., 2000a,b; Hadi et al., 2013) that would not occur in a smectite natively occurring in the ferrous state. Laboratory synthesis studies also constrain physical conditions, such as temperature and pH, that control cation solubility into the smectite structure along binary solutions (Decarreau et al. 2008; Andrieux and Petit 2010).

The ability to determine the conditions in which a smectite mineral formed, including the aqueous geochemistry and oxidation state, and by proxy the potential for habitability, is limited by the ability to accurately identify and measure smectite composition and mineral assemblages. Detailed characterization of the full compositional range of smectite minerals using techniques analogous to those employed in planetary exploration will help improve these capabilities for identification and compositional quantification. Here, we synthesize and report on the spectroscopic properties of a suite of smectite samples that span the intermediate compositional range between Fe, Mg, and Al end-member species, including both Fe(III)- and Fe(II)-dominated samples, using bulk chemical analyses, x-ray diffraction, Vis/IR reflectance spectroscopy, UV and green-laser Raman

spectroscopy, and Mössbauer spectroscopy. All spectra and patterns are available in the Supplementary Material.

2. Methods

2.1. Smectite Synthesis

Synthetic smectites were produced at Washington University using a hydrothermal sol-gel method modified from previous studies (Decarreau and Bonnin 1986; Chemtob et al. 2015). Solutions of magnesium, aluminum, iron(III), and iron(II) chlorides as well as sodium silicate were prepared from ultrapure deionized water (>18.2 MΩ cm). These solutions were mixed in stoichiometric proportions corresponding to the target smectite composition. Mg, Al and Fe(II/III) solutions were mixed first as these are acidic in nature, followed by the addition of the alkaline sodium silicate solution. Upon mixing these solutions quickly precipitated a gel, which were then were aged for 24 hours and centrifuged for 30 minutes at 16500 RPM in sealed tubes. The supernatant fluid was removed, and the gel was resuspended in ultrapure water and centrifuged again in order to remove excess salt. The gel was again resuspended in ultrapure water and the pH was adjusted to 9 using hydrochloric acid or sodium hydroxide. All steps in syntheses involving Fe(II) were conducted in an anaerobic chamber (Coy Laboratory Products) filled with a 97% N_2/3% H_2 mixture and a catalyst system that decomposes O_2 using the excess hydrogen in the chamber.

184

185 After pH adjustment the gel suspensions were placed into PTFE-lined Parr acid
186 digestion vessels and heated in an oven at 200°C for 15 days. To prevent oxidation
187 during heating, the syntheses involving Fe(II) were heated in a vacuum oven
188 backfilled with ultrahigh purity nitrogen gas. After cooling to room temperature, the
189 smectites were immersed in a 0.5 M calcium chloride solution for several hours to
190 Ca-saturate the interlayer via cation exchange, before being washed once more with
191 ultrapure water and dried in a vacuum desiccator. Some of the Fe(III)-bearing
192 samples were incompletely dried, such that during subsequent storage for ~12
193 months, some samples formed minor calcite impurities. These growths were
194 identified by comparing X-Ray diffraction (XRD) patterns collected before and after
195 storage. We attribute the calcite impurities to CO_2(g) taken up by the excess water in
196 the samples reacting with interlayer Ca during gradual dehydration during storage.
197 These calcite impurities were removed by suspending the sample for 30 minutes in
198 a pH 5 sodium acetate-acetic acid solution at 80°C (Ulery and Drees 2008).
199 Following this treatment, the smectites were again Ca saturated, washed and dried.

200

201 2.2. Chemical Analysis

202

203 Elemental abundances were determined using ~50 mg of each synthetic smectite.
204 These were first gently crushed with an agate mortar and pestle and added to a
205 graphite crucible with 350 mg of lithium metaborate flux. The mixture was fused
206 into a glass bead by heating in a muffle furnace at 1050˚C for 15 minutes. The glass

beads were dissolved in 40 ml of 10% nitric acid, followed by a 1:100 dilution in 2% nitric acid. The diluted samples were analyzed by inductively coupled plasma optical emission spectroscopy (ICP-OES) using a Perkin Elmer Optima 7300DV instrument.

Structural formulae for the smectites were constructed by taking the molar abundances of each of the cations and normalizing their total positive charge against the twenty-two units of negative charge in the half-unit cell formula. All Ca and Na is assigned to the interlayer. All Si is then assigned to the tetrahedral sheet, as is additional Al to bring the tetrahedral sheet to full occupancy at 4 atoms per half-unit cell. For select Fe(III)-rich samples, Al is insufficient to fill the tetrahedral sheet and Fe(III) is then used to provide full occupancy. The remaining Al, Fe and Mg are then assigned to the octahedral sheet. For the samples containing Fe(II), past syntheses have shown that minor Fe(II) oxidation may occur because of the difficulty in preventing any exposure to air during brief transfers between an anaerobic chamber and vacuum oven. The fraction of iron in the ferrous form [Fe(II)/Total Fe] was determined by digestion of a subsample in 10 g/L ammonium bifluoride followed by complexation of Fe(II) by 1,10-phenanthroline(Tarafder and Thakur 2013). The Fe(II) concentration was then determined by measuring the absorbance at 510 nm using an ultraviolet-visible spectrophotometer (Thermo Scientific Evolution 60). These assays were only performed for syntheses involving Fe(II), as the Fe(III) syntheses products at no point were exposed to chemical reductants.

230 2.3. X-Ray Diffraction

231

232 Powder XRD patterns were collected on a Bruker D8 Advance diffractometer
233 equipped with a LynxEye XE energy-dispersive strip detector. Samples were gently
234 ground in an agate mortar and pestle and placed into a silicon zero background
235 sample holder for measurement. Samples containing Fe(II) were also enclosed in a
236 air-tight dome to prevent oxidation during measurements, although this produced a
237 large scattering feature between approximately 8° and 18° 2θ. Data were collected
238 using Cu K_α radiation (40 kV, 40 mA) from 3° to 65° 2θ with a 0.015° step size and a
239 0.8 second collection time per step. A continuous scanning data collection mode was
240 employed with the total counts at each data point representing the sum of the
241 counts measured as each of the 192 strips of the detector were swept through the
242 corresponding 2θ position, yielding a total counting time per point of 153.6 s.

243

244 The XRD data were analyzed for both peak positions and lattice parameters, as
245 the asymmetric nature of the turbostratic scattering bands make structural analysis
246 from peak positions alone inaccurate (Moore and Reynolds 1997). The positions of
247 the (001), (02,11) and (06,33) peaks were determined using least squares fitting of
248 a single pseudo-Voigt profile and a linear background. Lattice parameter
249 refinements were conducted using the Profex interface (Doebelin and Kleeberg
250 2015) to BGMN (Bergmann et al. 1998). This employed the approach of Ufer et al.
251 (2004) to simulate the smectite X-ray scattering pattern, with the structure
252 modified to match the compositions determined by sample digestion. The *c* lattice

parameter was obtained through refinement to the (001) feature between 3° and 8° 2θ. For the in-sheet lattice parameters, a hexagonal sheet symmetry was assumed, fixing $a = b/\sqrt{3}$. The (02,11) and (06,33) bands were fit separately, from 18° to 21.5° 2θ and 57° to 64° 2θ, respectively. *b* lattice parameters are thus reported for each peak refinement. Corresponding d-spacings associated with diffraction features were then calculated from both the lattice parameters and peak positions for comparison. For the latter, the weighted average wavelength of 1.5418 Å for Cu $K_{\alpha 1,2}$ radiation was used. This wavelength, along with 1.7903 Å for Co $K_{\alpha 1,2}$, was used for peak position conversions between common X-ray tube wavelengths.

2.4. Visible to Near Infrared Spectroscopy

Visible/near infrared reflectance (VNIR) spectra were acquired at wavelengths from 350 to 2500 nanometers and a spectral resolution of 6 nm using an Analytical Spectral Devices (ASD) Fieldspec3 with a 5˚ field of view and a custom goniometer device at Caltech. The samples were illuminated using a halogen light source placed at a 30˚ angle, and the fiber optic was positioned normal to the sample surface. The collected samples were calibrated by making measurements relative to a NIST-certified spectralon reflectance standard and correcting for its known properties. The bidirectional reflectances in the Supplementary Materials can thus be considered absolute reflectances. Samples were ground and sieved to particulate sizes less than 120 μm to reduce shadowing effects from larger grains sizes. Fe(II)-bearing samples were measured in a dry Ar atmosphere within an anoxic glovebox.

276

277 2.5. Mid-Infrared Spectroscopy

278

279 Mid-infrared diffuse reflectance spectra were acquired on a Thermo Scientific
280 Nicolet iS50 transform infrared spectrometer with a 4 cm^{-1} sampling interval and
281 averaged 512 scans. Fe(III)-bearing samples were placed in a dry air-purged sample
282 chamber to acquire diffuse reflectance measurements over 5000-400 cm^{-1} (2-25
283 μm). The system was purged with dry N_2 during measurements of the Fe(II)-bearing
284 samples. The system was calibrated using a rough Al target, which was assumed to
285 have a reflectance of unity. (Any investigations requiring absolute reflectance and
286 utilizing the Supplementary Material should scale MIR to Vis/NIR data values).

287

288 Each sample was also measured using the SensIR Durascope attenuated total
289 reflectance accessory on a Nicolet Magna 860 Fourier transform infrared
290 spectrometer. Powdered samples were pressed against a diamond crystal and
291 spectra were acquired over 4000 - 400 cm^{-1}, (2.5-25 μm) using a KBr beam splitter
292 and an uncooled triglycine sulfate detector with a KBr window. Background
293 calibration spectra were acquired using the diamond crystal alone. All samples were
294 measured in air, as oxidation during the short integration times (<3 minutes) is
295 considered negligible and the sample size required is small.

296

297 2.6. Raman Spectroscopy

298

299 Raman patterns were collected on loosely packed powdered samples on a
300 Renishaw M1000 micro Raman spectrometer using a 532-nm solid state 100 mW
301 laser with a 2400 nm diffraction grating on loosely-packed powdered sample and a
302 spot size of 100 μm. The laser power was attenuated to 10% to avoid ablating the
303 samples, and scans were averaged to improve counting statistics. Spectra were
304 collected between 100 and 4000 cm^{-1} with a 1 cm^{-1} sampling interval. Wavelength
305 accuracy was calibrated using a silicon chip to within 0.5 cm^{-1}. Spectra were
306 background corrected using a cubic spline interpolation. All samples were measured
307 in air. Exposure of the Fe(II) samples was minimized prior to measurement, and
308 oxidation during the <8 minute exposure times is considered minimal. The 532 nm
309 excitation wavelength is equivalent to the Raman spectrometry system planned for
310 the SuperCam instrument designed for the Mars 2020 rover mission (Wiens et al.
311 2017).
312
313 Deep-ultraviolet (DUV) Raman spectra were obtained using MOBIUS (Mineralogy
314 and Organic Based Investigations Using Ultraviolet Spectroscopy), the laboratory
315 prototype for the SHERLOC instrument (Scanning Habitable Environments with
316 Raman and Luminescence for Organics and Chemicals) designed for the Mars 2020
317 rover mission (Beegle et al. 2017). Measurements were done using a 248.58 nm
318 pulsed laser (Photon Systems, Inc) with a focused spot diameter of ~40 μm, an 1800
319 lines/mm diffraction grating and a Horiba Symphony e2v 42-10 CCD liquid nitrogen
320 cooled (−140 °C) detector. Each spectrum was acquired over 30 seconds at a pulse
321 rate of 40 Hz, totaling 1200 pulses. Spectra were collected between over 1024

322 points between ~570 cm^{-1} and ~4200 cm^{-1} with a spectral accuracy of 3.8 cm^{-1}, and
323 wavelengths were calibrated using validating the position of the primary and
324 secondary laser lines at 248.58 and 252.93 nm respectively. For each sample of
325 loosely packed powder, 25 spectra were obtained in a 5x5 array with a spacing of
326 100 μm. Cosmic rays were identified as outliers in the distribution of intensity
327 values in each Raman shift channel and replaced by the value of adjacent points
328 (Uckert et al. 2019). Further processing was done by in-house Python scripts
329 utilizing publicly available packages Numpy, SciPy, and LMFIT (van de Walt et al.,
330 2011; Jones et al., 2001; Newville et al., 2014). Processing included subtraction of a
331 linear baseline by least-squares regression, a recalibration of Raman shift values
332 based on the position of the atmospheric N_2 peak relative to its literature position of
333 2331 cm^{-1}, and subsequent removal of atmospheric N_2 and O_2 peaks by subtraction
334 of a standard atmospheric Raman spectrum acquired on the same spectrometer.
335 The processed spectra were normalized with respect to the N_2 peak amplitude and
336 peak positions, FWHM, and intensities were determined by fitting with gaussian
337 functions.
338
339 2.7. Mössbauer Spectroscopy
340
341 Mössbauer spectra were recorded on a spectrometer from SEE Co. operating in
342 the constant acceleration mode in a transmission geometry. Samples were ground in
343 an agate mortar and, depending on the Fe content, 20-60 mg were added to 500 mg
344 boron nitride and mixed in a glass vial to create a homogenous sample (Table S4).

345 The resulting mixture was added to a Delrin cup, capped and measured. Spectra
346 were recorded with the temperature maintained using an SVT-400 Dewar from
347 Janis. The quoted isomer shifts are relative to the centroid of the spectrum of a
348 metallic foil of α-Fe at room temperature. Data analysis was performed using the
349 program WMOSS (www.wmoss.org) and quadrupole doublets were fit to Voigt
350 lineshapes.
351
352 3. Results and Discussion
353
354 3.1. Elemental Abundance of synthesized smectites
355
356 Ten Fe(III)-bearing smectites and six Fe(II)-bearing smectites were synthesized
357 with compositions intermediate to widely used standards (Figure 2). In calculations
358 of structural formulae (Table1), Fe(III) was required to fill the tetrahedral sheet in
359 the two most Fe(III)-rich compositions (samples A and B). Mg content was reduced
360 relative to Fe and Al in each of the final compositions compared to the initial
361 solution, matching observations of other smectite syntheses and suggesting higher
362 Mg solubility than Fe or Al in this system (Chemtob et al. 2015). Octahedral
363 occupancies per half-cell derived from the structural formula (Table 1) indicates
364 that the Fe(III) smectites are generally dioctahedral in nature with the exception of
365 samples G, H, and J, which have formulas suggestive of di-trioctahedral clays. Fe(II)
366 smectite compositions suggest trioctahedral compositions similar to those studied
367 by Chemtob et al. (2015), except for two Al-rich compositions (N and O). Samples K,

L, M and P are consistent with trioctahedral Fe(II)-Mg smectites, sample N is dioctahedral and sample O is a di-trioctahedral smectite. Seven to 15% of the iron in the Fe(II) smectites oxidized during synthesis (Table 1), which is attributed to leakage of small quantities of O_2 into the vacuum oven during synthesis or from leakage into the anaerobic chamber during pre- or post-synthesis treatments.

3.2. X-Ray Diffraction

The XRD patterns (Figure 3) of the synthesized clays confirm that all are smectites, with broad asymmetrical features that are indicative of turbostratic stacking. No other crystalline phases are present except for in sample L, which has <0.4 wt.% quartz (determined by Rietveld refinement) which is attributed to contamination during sample preparation for XRD or present in the sample holder. The (001) diffraction peaks near 6° 2θ (Table 2) correspond to basal layer spacings between 13 and 17 Å (Table 3), consistent with 1 to 3 layers of water in the interlayer. Table 2 also shows the equivalent peak position for each feature if measured by Co K_α radiation, as done onboard the Mars Science Laboratory CheMin XRD instrument. The relatively weak and broad (001) reflections are often observed in XRD patterns of synthetic smectites (Grauby et al. 1993, 1994; Chemtob et al. 2015) and indicate small coherent domain sizes, i.e., a small number of stacked layers per crystallite. The peak between 25 to 30° 2θ is primarily the (003) reflection, which like the (001) feature is broad because of the small coherent domain size (Figure 3a). This feature also includes scattering from some water associated with the samples (Morgan and Warren 1938). The remaining features are

391 (hk) peaks associated with X-ray scattering from within the smectite sheet (Brindley
392 and Brown 1980; Moore and Reynolds 1997).
393
394 The (060) d-spacing, typically calculated from the peak position of the (06,33)
395 band near 60˚ 2θ (Table 3, Figure 3c), is most commonly used to determine unit cell
396 dimensions. This is also typically considered diagnostic of dioctahedral versus
397 trioctahedral structures, although, as our results show, there is overlap in the range
398 of values for these features once the diversity of compositions is considered. The
399 Fe(III) smectites in this study (samples A-J) have (060) d-spacings between 1.520
400 and 1.528 Å based on peak positions. The Fe(II) smectites show a much broader
401 range, from 1.516 to 1.557 Å, consistent with prior work (Chemtob et al. 2015).
402 Three of the Fe(II) smectites (K, N, and O) have splittings in the (06,33) peaks that
403 suggest the presence of separate domains of distinct clay compositions intermixed
404 among the layers, which has been observed to occur in previous syntheses of Fe(II)
405 smectites (Chemtob et al. 2015), as well as other smectite compositions (Grauby et
406 al, 1993). The shoulder feature for sample K may indicate an anomalously long d-
407 spacing (~1.58 Å) but the exact origin of this feature is uncertain as the dome used
408 to seal the sample also produce an increase in background scattering near this
409 feature. The splittings in the (06,33) peak for samples N and O are clearer in nature
410 and suggest mixtures of trioctahedral and dioctahedral domains. This parallels a
411 miscibility gap previously reported for the Mg saponite-beidellite series (Grauby et
412 al. 1993), suggesting that Fe(II) saponites also display such a gap as Al content
413 increases. Peak positions of the (02,11) peak similarly show small variation among

414 the Fe(III) smectites and much larger variations among the Fe(II) smectites (Table
415 2, Figure 3b). The derived lattice spacing, as calculated from peak refinement,
416 reflects octahedral coordination state (Figure 3d). Dioctahedral sample basal
417 spacings exhibit little dependence on Fe(III) octahedral content (Figure 3e), but tri
418 and di-trioctahedrally coordinated samples demonstrate a more linear trend
419 towards increasing d-spacing with increasing octahedral Fe (both Fe(II) and Fe(III)).
420
421 Lattice parameters were refined for both Fe(III) and Fe(II) smectites using a
422 single smectite structure to model both the (02,11) and (06,33) peaks, and thus
423 obtained one *b* value from each, even when peak splitting was observed (Table 3).
424 Calculation of the (060) d-spacings from lattice parameters obtains values ~0.004 Å
425 larger than values determined from peak positions (Table 4). This discrepancy is
426 real and results from smectite sheets scattering as 2-dimensional crystals, with peak
427 positions occurring at slightly higher angles in 2θ than the actual (06,33) position
428 (Brindley and Brown 1980; Moore and Reynolds 1997). Lattice parameter
429 refinements of the (02,11) show similar trends in *b* values as the peak positions.
430 However, the discrepancy between the d-spacing as derived from the peak position
431 and the lattice parameter is an order of magnitude larger in this case, with peak
432 positions underestimating actual d-spacings by 0.04 to 0.07 Å. While this is a long
433 established aspects of the X-ray scattering properties of turbostratic smectites, this
434 is again emphasized here because the (02,11) peak is the primary structural
435 features observable in X-ray diffraction patterns collected by the MSL rover, as the
436 (06,33) peak is outside of the angular range of the instrument.

437

438 3.3. Visible to Near Infrared Spectroscopy

439

440 Spectral features in the Visible to Near Infrared (VNIR) wavelength region are
441 caused by electronic absorptions related to charge transfer and crystal field
442 splitting, as well as the overtones and combinations of the fundamental vibrational
443 modes of the chemical bonds within a mineral structure, such that the wavelength
444 position of absorption features provides characteristic information about the
445 mineral composition (Gates et al. 2017). The reflectance also depends on the
446 particle size and viewing geometry of the samples under investigation. The VNIR
447 reflectances of the synthetic smectite samples exhibit absorptions caused by
448 electronic transitions in Fe(II) and Fe(III), and cation-OH bending and stretching
449 modes between 0.5 and 2.5 μm (Figure 4).

450

451 In the visible and short-wavelength near infrared (0.4-1 μm), Fe crystal field
452 absorptions dominate the spectral shape. Within the Fe(III) samples, overlapping
453 ferric features dominate the spectrum between 0.4 and 1 μm, but vary as a function
454 of Fe content. Fe(III)-bearing samples A-J all have a spectral maximum near 0.76
455 μm. The positive spectral slope from 0.4-0.76μm observed in all Fe(III)-bearing
456 samples is caused by charge transfer bands that are centered in the UV and the
457 broad 0.60μm and 0.96μm absorptions, attributed to electron transitions in the
458 Fe(III) ions in the octahedral structure (Hunt 1977). A narrower feature centered at
459 0.48μm is also an Fe(III) charge transfer absorption (Rossman 1976; Hunt 1977).

460 The 0.96 μm absorption is present in all samples save sample J, which only has 9%
461 octahedral Fe(III). The 0.48 μm absorption is most pronounced in samples with
462 relatively less Fe(III) content, which is consistent with an enhanced charge transfer
463 absorption due to substitution of a 3+ ion into a 2+ crystal site (Burns 1970; Hunt
464 1977). The Fe(II)-bearing samples have a distinctly different spectral shape in the
465 visible and near infrared due to Fe(II) electronic absorptions. Samples K-P have a
466 spectral maximum at 0.5 μm, and very broad absorption features centered around
467 0.72, 0.88-0.92 and 1.11-1.13 μm, attributed to Fe(II) crystal field absorptions (Hunt
468 1977; Bishop et al. 2008c).
469
470 All samples have broad, asymmetrical absorptions centered at 1.91 μm, caused by
471 the combination of bending and stretching modes of H_2O molecules within the
472 mineral structure. The interlayer of smectite clays can accommodate significant
473 molecular substitution, such that ambient humidity affects H_2O absorption into the
474 mineral structure. The depth and structure of the 1.91μm absorption feature is a
475 function of the samples' hydration; a shoulder around 1.97 μm that occurs in some
476 samples indicates the presence of relatively more absorbed water in the interlayer
477 (Bishop et al. 1994). The combination of the symmetric and asymmetric stretch
478 together with the H_2O bending mode occurs at 1.15 μm, and is detectable in the
479 Fe(III)-bearing samples. Sample J, which has the least strong Fe electron features,
480 also shows the second overtone of the H_2O stretching mode at 0.97 μm, which is
481 obscured by the stronger Fe absorptions in the other samples. The 0.97 and 1.15μm
482 absorptions are not apparent in the Fe(II)-bearing samples, likely due to the

483 stronger overlapping Fe(II) electronic features. All samples also exhibit a strong
484 absorption centered near 1.41 μm due to the first overtone of the structural OH and
485 H_2O, and a shoulder at 1.46 μm is attributed to a more H_2O saturated interlayer
486 (Bishop et al. 1994). Structure within this absorption is due to overtones of the
487 Metal-OH (M-OH) stretching and bending modes observed at longer wavelengths.
488 Samples H and J and P, with the most octahedral Mg, have a band at 1.395 μm,
489 compared to all other more Fe rich samples which have absorptions centered
490 towards 1.43 μm, consistent with prior work (Madejová et al. 2000).
491
492 The NIR region between 2.1 and 2.5 μm is particularly diagnostic of smectite clay
493 composition as absorptions caused by the combination of the bending and
494 stretching modes of the octahedral cations and hydroxyl molecules occur in this
495 range. The intensities and center positions of these absorptions shift as a function of
496 the relative abundance of Fe(III), Fe(II), Al, and Mg in the octahedral layer (Figure
497 5). Samples with high octahedral Al contents show absorption features in the 2.20-
498 2.25μm range (Figure 5a). In the Fe(III) bearing samples C, D, H and I, shallow and
499 broad absorptions around 2.23μm are combination absorptions attributable to Al-
500 Fe(III)-OH and Al-Mg-OH bending and stretching modes. The Al-related absorptions
501 are more well defined in the Fe(II) bearing samples; a narrow absorption feature
502 shifts from 2.25μm in the most Fe(II) rich samples to 2.23μm in the Fe(II) poor (Mg-
503 rich) samples. Samples O and N, which are the most Al rich samples in the suite, also
504 have well defined Al-Al-OH absorptions at 2.20μm. All of the Fe(III)-bearing samples
505 have distinct absorptions centered at 2.28 μm caused by combination of the $Fe(III)_2$-

506 OH bending and stretching vibrational modes that occur in the mid-infrared (Figure
507 5b) (Madejová et al. 2000; Gates 2005). Samples H and J also have an absorption
508 center at 2.31 μm attributed to the Mg-OH-Mg combination absorption (Grauby et al.
509 1994). Sample K has a dominant absorption at 2.35μm attributed to $Fe(II)_2$-OH
510 combination modes, and the position of this feature shifts to 2.33μm in samples L
511 and M as Fe(II) in the octahedral sheets decreases. Samples N and O lack a defined
512 absorption feature in this wavelength range and have only a shallow shoulder near
513 2.33μm. Sample P has an asymmetric absorption at 2.32, consistent with the low Fe
514 and high Mg octahedral sheet content in this sample.
515
516 The Fe(III)-bearing samples have an absorption band that does not shift
517 significantly as a function of composition at ~2.39μm. It is most strongly defined in
518 samples J, H, A and B, but is detectable in all of the spectra. This feature is attributed
519 to the combination of cation-OH stretches in the octahedral sheets and the
520 tetrahedral Si-O stretch(Gates 2005). Mg-dominated samples H and J have a
521 narrower, more pronounced absorption compared to the wider features in the more
522 Fe(III) dominated samples. The more aluminous samples, C, D, G, I, N and O,
523 together with all of the Fe(II)-bearing samples, have broad bands with centers
524 shifted towards 2.45μm. In the Fe(II)-bearing samples, this shift is approximately
525 linear as a function of Mg content, although the Fe(III) samples do not show well
526 defined compositional dependence (Fig 5c).
527
528 3.4. Mid-Infrared Spectroscopy

529

530 3.4.1. Attenuated Total Reflectance

531

532 The Attenuated Total Reflectance spectra of the suite of ferruginous smectites are
533 shown in Figure 6, and assignments are made based on previous works. Peaks in the
534 ATR spectra are primarily a function of the absorption coefficient of the material
535 and peaks in the 400-4000 cm^{-1} range are caused by the fundamental molecular
536 vibrational modes. Higher degrees of crystallographic symmetry sharpen peaks,
537 whereas less-ordered structures and overlapping vibrational modes produce broad
538 peaks. Generally, octahedral OH stretching modes occur between 3800-3000 cm^{-1}
539 (2.63-3.33μm) (Figure 6a), and the octahedral OH bending modes, together with the
540 tetrahedral stretching and bending modes, occur between 1200-400 cm^{-1} (8.33-
541 25μm) (Figure 6b).

542

543 All samples have well defined features between 3800-3000 cm^{-1} (2.63-3.33μm)
544 that are caused by H_2O related vibrational modes and cation-OH stretching modes. A
545 shoulder feature that occurs 3220 cm^{-1} (3.1 μm) is the first overtone of the H_2O
546 bending mode that occurs in all samples at 1635cm^{-1} (6.12μm) (Clark et al. 1990;
547 Bishop et al. 1994; Madejová et al. 2002). A broad peak centered around 3390 cm^{-1}
548 (2.94 μm) is attributed outer-sphere H_2O bonding within the interlayer; its strength
549 has been correlated with the hydration levels of the smectite (Bishop et al. 1994;
550 Madejová et al. 1994), and its relative strength among samples measured here also
551 tracks with observed trends in the near-infrared that suggest that some of the

552 samples are more hydrated than others. Peak and shoulder features between 3700-
553 3550cm^{-1} (2.70-2.81μm) are attributed to cation-OH stretching modes. Samples A-F
554 have a peak feature, most clearly observed in samples A and B, at 3550cm^{-1}
555 (2.81μm) that is associated with $Fe(III)_2$-OH stretching (Gates 2005). Samples I and J
556 have a well-defined shoulder feature at 3680cm^{-1} (2.71μm) that is ascribed to the
557 Mg_2-OH stretching vibration (Grauby et al. 1994). A shoulder at 3630 cm^{-1} (2.75μm)
558 is prominent in almost all of the samples, and is the dominant feature in the Fe(II)-
559 bearing samples (Figure 6a). This is most consistent with features that have been
560 attributed to Al_2-OH or Al-M-OH bending modes in other smectite samples (Grauby
561 et al. 1993; Madejová et al. 1994; Gates 2005) and is likely the cause in these
562 samples. The $Fe(II)_2$-OH absorption would be expected at lower wavenumbers
563 (higher wavelengths) than the $Fe(III)_2$-OH absorptions (Gates 2005), but no such
564 feature is observed in the ATR spectra of the Fe(II)-bearing samples, likely due to
565 stronger overlapping H_2O features.
566
567 The tetrahedral Si-O stretching and bending modes occur between 400 and 1200
568 cm^{-1} (Figure 6b). In all of the ferruginous smectite samples, the Si-O stretching mode
569 in the tetrahedral sheet occurs around 985 cm^{-1}, and the Si-O-Si bending mode
570 occurs between 415-440cm^{-1} in the Fe(III) bearing samples and 430-460cm^{-1} in the
571 Fe(II) bearing samples. The stretching mode does not demonstrate a significant
572 dependence on composition, but the bending mode moves to longer wavenumbers
573 as Fe content increases in all samples. A band near 485 cm^{-1} attributed to the
574 $Fe(III)_{oct}$-O-Si_{tet} bending mode is apparent in samples with at least 30% Fe(III); the

575 shoulder shifts to 510 cm^{-1} in samples C, D, G and I with an increase in Al in the
576 octahedral sheet, implying the presence of an Al-O-Si bending mode(Madejová and
577 Pálková 2017). The feature around 515cm^{-1} in the more aluminous Fe(II)-bearing
578 samples M, N and P is also ascribed to the same Al-O-Si bending mode.
579
580 The fundamental octahedral cation-OH bending modes also occur in the same
581 region as the Si-O fundamental absorptions. An asymmetric band at 680 cm^{-1},
582 present in all of the Fe(III)-bearing samples, is attributed to interactions between
583 the bending of the Fe-O out of plane bend and Si-O vibrations, and in more tri-
584 octahedral samples H and J overlaps the Mg_2-OH bend at 656 cm^{-1} (Grauby et al.
585 1994; Frost and Kloprogge 2000b; Gates 2005). The Fe(II)-bearing samples have
586 less well defined features in this region than the Fe(III)-bearing samples, but have a
587 very broad plateau between 658-570cm^{-1} caused by overlapping Mg_2-OH, Fe(II)-
588 Fe(III)-OH and $Fe(II)_2$-OH bending modes that are not well distinguished. The
589 Fe(III)-bearing samples also exhibit a pair of bands at 815-817 and 870 cm^{-1} that are
590 attributed to the $Fe(III)_2$-OH and the Fe(III)-Al-OH bends (Grauby et al. 1994; Gates
591 2005; Andrieux and Petit 2010). The 817 cm^{-1} band is only apparent in samples A-E
592 and disappears with decreasing Fe. The Fe-Al-OH bend is also detectable in the
593 Fe(II) bearing samples, although it has reduced spectral contrast.
594
595 3.4.2. Diffuse Infrared Reflectance
596

Similar to reflectance spectra in the visible and near infrared, mid-infrared reflectance spectra depend on both the real and imaginary component of the complex index of refraction. However, while the real component is relatively constant from the visible out to about 5-6 μm such that spectra in the visible to near infrared are practically a function of only the variation in the imaginary component, both the real and imaginary components vary significantly through the infrared region, causing both reflectance minima and maxima that are telling of the mineralogy. Spectral features between ~4000 and 100 cm^{-1} (2.5-25 μm) are caused by the fundamental bending and stretching modes of hydroxyl bonds in the octahedral sheets and silicate structures in the tetrahedral sheets, as well as molecular water within the structure (Figure 7).

As in the ATR spectra, the presence of interlayer and adsorbed H_2O causes the deep, broad absorptions centered at 2.94μm (3400cm^{-1}) and 3.12μm (3200cm^{-1}) (Clark et al. 1990; Bishop et al. 1994). The depth of this feature is dependent on the abundance of water molecules within the interlayer. Superimposed on the fundamental H_2O stretches are the narrower stretching modes of the cations bound to the hydroxyl molecules within the octahedral sheets (Figure 7a). In the Fe(III) samples, absorption minima shift from ~2.79 to 2.75μm with decreasing Fe(III) content (Figure 7b). All samples except for H and J have the deepest metal-OH stretching minimum between 2.80-2.82μm (3560-3540cm^{-1}), consistent with Fe(III) being the controlling cation in the octahedral sheets. The $Fe(III)_2$-OH stretch occurs at 2.80μm (3560 cm^{-1}) (Madejová et al. 1994) and is most prominent in samples A

620 and B. Samples C, D, E and F have band minima shifted approximately linearly
621 towards 2.75μm (3635 cm^{-1}) due to the presence of aluminum and the Al_2-OH
622 stretching mode. Samples H and J, having the least Fe(III) within the octahedral
623 sheets, show distinct, narrow minima at 2.721μm (3674 cm^{-1}), which are attributed
624 to the Mg-OH-Mg stretching modes. As with the Fe(III)-bearing samples, the minima
625 of the Fe(II)-bearing samples also shift linearly to longer wavelengths and shorter
626 wavenumbers with increasing Fe(II) from 2.72-2.76μm (3680-3624cm^{-1}) (Figure
627 7b).
628
629 The mid-infrared region between 100 and 1200 cm^{-1} contains information about
630 both the octahedral and tetrahedral sheets, as both the fundamental bending modes
631 of the octahedral cation-OH bonds and the bending and stretching modes of the Si-O
632 bonds in the tetrahedral sheet occur in this range (Figure 8). Features are similar to
633 those observed in the ATR spectra, although the band positions are shifted, and as
634 the reflectance is sensitive to both the absorption and scattering coefficients, display
635 features related to changes in both the real and imaginary component of the index of
636 refraction. All samples have a strong peak centered between 1030-1045cm^{-1} that is
637 attributed to the fundamental Si-O stretch. The position of this feature does not
638 demonstrate a clear trend as a function of composition in the Fe(III)-bearing
639 samples, but does shift to larger wavenumbers in the more aluminous Fe(II)-bearing
640 samples (Figure 8d). A peak around 455 cm^{-1}, which ranges from 410 to 480 cm^{-1}
641 with decreasing Fe, is attributed to the Si-O bending mode (Frost and Kloprogge
642 2000b) (Figure 8b). The dioctahedral samples A, B, C, D, E, F, and G all have

643 secondary peaks between 490-510cm^{-1}; samples A and B in particular have the most
644 distinct secondary peaks centered at 500 cm^{-1}, attributed to the Fe(III)$_{tet}$-O-Si
645 bending modes, due to Fe substitution into the tetrahedral sheet (Frost and
646 Kloprogge 2000b; Madejová and Pálková 2017). The secondary peaks in the other
647 dioctahedral samples are weaker relative to the tetrahedral Fe(III) as they are
648 caused by out of plane Fe-O bend, between the tetrahedral and octahedral sheets.
649 The trioctahedrally-coordinated samples, particularly H and J, typically show only a
650 single Si-O bending peak, but have a pronounced shoulder near 530 cm^{-1} attributed
651 to the Mg-O out of plane bending mode (Gates et al. 2017). Samples N and O in the
652 Fe(II)-bearing samples appear double peaked in this spectral region, consistent with
653 the peak splitting of the (06,33) peak in the XRD indicating multiple clay domains,
654 i.e., a partial trioctahedral and dioctahedral nature.
655
656 The fundamental bending modes of the octahedral cation-OH bonds occur
657 between 600 and 1000 cm^{-1}. All of the Fe(III)-bearing samples have a broad band
658 near 845cm^{-1} that does not manifest in the Fe(II)-bearing samples. This bending
659 feature is assigned to Fe(III)$_2$-OH in the dioctahedral samples and Fe-Mg-OH in the
660 trioctahedral Fe(III)-bearing samples (Keeling et al. 2000; Gates 2005). The peak
661 center shifts to shorter wavenumbers as the Mg content of the samples increase and
662 the Fe content decreases (Figure 8c). Samples A-D also have a have a shallow, broad
663 peak near 906 cm^{-1} which is attributed to the Al-OH-Fe(III) bending mode (Andrieux
664 and Petit 2010).
665

Samples A – G have a low-intensity, very broad plateau between 745-802 cm^{-1} caused by overlapping contributions of OH bending modes and tetrahedral Si vibrations (Gates 2005). The shoulders are better resolved as a function of increasing Fe content; the bands associated with the feature are the Fe-Al-OH and Fe-Mg-OH bends, which are broadened by lattice deformations caused by irregular cation substitution (Grauby et al. 1994; Gates 2005; Andrieux and Petit 2010). All samples save O and N exhibit a weak Fe-O out of plane bending mode between octahedral Fe and Al and the bridging oxygen that contributes to an asymmetrical, broad peak around 687cm^{-1} (Grauby et al. 1994; Gates 2005). This feature overlaps with the Mg-Mg-OH bend that occurs closer to 630cm^{-1}, which is most apparent in samples H, J.

3.5. Raman Spectroscopy

Raman spectroscopy probes the vibrational modes within the mineral structure, similar to IR spectroscopy methods, but not all bond structures are active in both the IR and Raman, so the two methods are frequently complementary. Like IR measurements, Raman spectroscopy is useful for identifying the stretching and bending modes of the octahedral M-OH interactions and the tetrahedral silicate structure. Smectite clays do not generally have strong Raman responses, due to the low crystallinity and small grain sizes that characterize clay minerals. In particular, the Fe(II)-bearing samples in this study have lower measured intensities and

greater photoluminescence effects that obscure features relative to the Fe(III)-bearing samples.

3.5.1. 532nm Green Raman

The Raman spectra produced using the 532nm excitation laser are shown in Figure 9. Most of the Raman peaks between 100 and 1100 cm^{-1} contain information about the tetrahedral bonds (Figure 9b). All of the samples have a peak near 185 cm^{-1}. It is sharply defined in the Fe(III) bearing samples and sample P, and is detectable but weaker in samples with increasing Fe(II) content. There is not a significant positional change as a function of composition (Figure 9d). Similar peaks near 187cm^{-1} observed in other nontronites were ascribed to an octahedral asymmetric $Fe(III)_{oct}$-O_{tet} stretching vibration (Frost and Kloprogge 2000a).

A pair of bands at 245 and 280 cm^{-1} occur in all of the Fe(III)-bearing samples (Figure 9b). In Fe(III)-rich samples, both peaks are evident, and the 245 cm^{-1} peak is better resolved, whereas in the trioctahedral sample J only the 280 cm^{-1} peak is detected. The intensity and FWHM of the 245 cm^{-1} peak decreases as Mg content increases. In the Fe(II)-bearing samples, peaks around 255cm^{-1} are poorly resolved in samples O and M, but the signal intensity in all of the Fe(II)-bearing clays make identification challenging. These features are attributed to a lattice deformation between the non-bridging oxygen atoms within the tetrahedral structure and the octahedral OH molecules (Frost and Kloprogge 2000a).

711

712 Peaks observed in the Fe(III) samples at 360, 465, and 676-687 cm^{-1} (Figure 9b) are
713 all associated with vibrational modes of the SiO_4 unit (Frost and Kloprogge 2000a).
714 The peak at 465 cm^{-1} can be resolved in all samples, although it is much weaker in
715 the Fe(II)-bearing samples due overlapping features at higher Raman shift, and does
716 not show a compositional dependence. The 465cm^{-1}feature is attributed to the Si-O
717 bending mode in the tetrahedral sheets. The ~680cm^{-1} feature in shifts in position
718 from longer to shorter wavenumbers as a function of decreasing Fe(III) content, and
719 occurs only as a weak shoulder in the Fe(II) bearing samples except in sample P
720 where it is well resolved. The 680cm^{-1} is attributed to Fe(III)-Si-O bending modes
721 between the octahedral and tetrahedral sheets.

722

723 Samples J and H have a sharply defined peak at 432cm^{-1} that is much weaker in the
724 rest of the Fe(III)-bearing samples and is not well resolved in the Fe(II)-bearing
725 samples (Figure 9b). It is plausible that this is a Mg-related feature, i.e. Mg-O or Mg-
726 OH, given that these two samples tend to exhibit Mg-related features in the IR that
727 are not observed in the other more Fe-rich samples. There is also a broad
728 absorption near 510cm^{-1} that is detected in all of the Fe(III)-bearing samples except
729 J, and is best defined in the aluminous-Fe(III) bearing samples. Its presence cannot
730 be confirmed in the Fe(II)-bearing samples due to a very broad peak around 600cm^{-1}
731 , which is the strongest feature in these samples. Weaker peaks around 600 cm^{-1}
732 are also detected in most of the Fe(III) bearing samples. The peak position of the
733 600cm^{-1} peak shifts to shorter wavenumbers with increasing Fe content, although

734 the trend is weak, and there is not a systematic variation in the 510cm^{-1} band
735 position as a function of composition. Due to the compositional dependencies, both
736 of these feature may be related to Fe and Al within the crystal structure (Bishop and
737 Murad 2004; Wang et al. 2015).
738
739 The octahedral bonds in phyllosilicates are weaker Raman scatters than the
740 tetrahedral silicate structures (Wang et al. 2015). Between 800-1000cm^{-1} there is
741 very low signal to noise and very broad features that are tentatively attributed to M-
742 OH bending modes (Bishop and Murad 2004) (Figure 9b). In samples A-F, there is a
743 shoulder feature near 885cm^{-1}, and in samples D, E and F the hump center shifts
744 towards 920cm^{-1}. Samples K-O also have very weak, broad features centered near
745 920cm^{-1}. These features may be consistent with the Al-Fe(III)-OH and Al-Al-OH
746 bending modes, respectively (Bishop and Murad 2004). The signal to noise is
747 insufficient to positively identify other features, as laser interference patterns,
748 particularly apparent in J and H, are on a similar intensity scale (Figure 9b).
749
750 The metal-OH stretching modes show a distinct compositional trend, and occur
751 between Raman shifts of 3500-3700 cm^{-1} as broad envelopes of overlapping peaks
752 (Figure 9c). Broader peaks caused by the Al-FeOH and Fe-FeOH stretches occur at
753 3630 and 3570 cm^{-1}, respectively, and are detected to varying degrees in all samples
754 except sample J. Sample P is the only Fe(II) bearing samples with detectable
755 stretching modes due to significant photoluminescence that dominated much of the
756 spectral range in the rest of the samples. Sample P has an overall shape consistent

with the Mg-rich samples H and J with the Mg-OH related shoulder at 3685 cm^{-1}, although the spectral contrast is reduced compared to the Fe(III)-bearing samples. A low, broad hump centered at 3400 cm^{-1} in most of the samples is attributed to an H_2O stretching mode, consistent with a hydrated interlayer, and is particularly apparent in samples H, I, J and K (de Ligny et al.,2013).

3.5.2. 248nm Deep-UV Raman

The DUV Raman spectra of the synthetic smectites (Figure 10a) begin at 800cm^{-1} due to the use of an edge filter to suppress a second laser emission line at 700 cm^{-1} (252.9 nm). Therefore, any lattice modes of tetrahedral SiO_4 unit or octahedral M-OH bending modes between 100-800cm^{-1} are not recorded. Every sample has a broad (FWHM of 120-300 cm^{-1}) peak feature at approximately 1065cm^{-1}, attributed to a Si-O stretching mode (Figure 10c). This peak varies between about 1055 and 1070cm^{-1}; although the Fe(III)-bearing samples do not demonstrate a clear compositional trend, the Fe(II)-bearing samples show a shift to longer wavelengths with increasing octahedral iron content. The presence of Fe in the samples also had a marked impact on the measured Raman intensity of this Si-O stretch; a clear trend is seen in the integrated peak intensity (after normalization to an internal standard, the atmospheric N_2 signal), which decreased with increasing Fe content (Figure 10d). This is not unexpected, as smectites are known to have UV absorption bands that are highly dependent on the concentration of octahedral Fe, particularly at ~250 nm, very close to the laser excitation wavelength (Chen *et al.*, 1979). However,

780 both samples J and O show less intensity than the trend would predict for Fe-poor
781 smectite. The intensity of sample P is also compromised by a strong Raman
782 reflectance peak near 1075cm^{-1} caused by minor calcite contamination that formed
783 after synthesis.
784
785 The Metal-OH stretching modes show demonstrable compositional trends (Figure
786 10b, 10e), and unlike in the Green Raman spectra, the Fe(II) bearing smectite
787 spectra are not photoluminescence dominated, such that stretching modes can be
788 detected. Samples J, P, O and N have a broad, multi-modal peak between 3300 and
789 3700 cm^{-1} consistent with the stretching mode of interlayer H_2O. These samples also
790 have distinct shoulders or superimposed peaks around 3660 and 3700cm^{-1}, which,
791 although shifted, are attributed to Mg and Al-OH stretching modes. Fe(III)-bearing
792 samples A-I, and Fe(II)-bearing samples K, L and M all have low intensity peaks that
793 vary between 3560 and 3620cm^{-1} with no systematic dependence on Fe or Al
794 content. This feature is attributed to Fe-OH stretching, although there is not a clear
795 distinction between Fe(III) and Fe(II) bonds.
796
797 A minor peak is observed at ~1600 cm^{-1} in all samples, although the intensity
798 relative to the 1050cm^{-1} peak varies widely and shows non-systematic
799 compositional trends (Figure 10a). This peak is not easily assigned, as few studies
800 for which Raman spectra are reported for smectites and other clay minerals have
801 considered the 1400-3000 cm^{-1} region (Frost and Kloprogge 2000; Wang et al.
802 2015). The peak occurs in the same frequency range as either an H_2O bending mode

or the C=C stretching mode (Ferrari and Robertson 2001; Bishop and Murad 2004; Socrates 2004), e.g., the 'G' band of carbonaceous material (Schopf et al. 2005; Quirico et al. 2009). As the H_2O content does not show large variation in the IR or Green Raman measurements, we tentatively assign the strongest ~1600cm^{-1} peaks to a possible organic contaminant, which may have been picked up during handling. Although a corresponding peak is not definitively observed under 532 nm excitation in samples other than P, N and M, selective detection of carbon-rich contaminants using 248 nm excitation can be attributed to resonant enhancement of C=C vibrations associated with π-π* absorption in the UV(Asher and Johnson 1984; Beegle et al. 2015; Sapers et al. 2019). Previous studies using the same UV Raman instrument have shown that the resonant Raman scattering from certain carbon-rich compounds, such as polycyclic aromatics, can be detected at concentrations as low as 0.1 ppm within mineral matrices (Abbey et al. 2017).

3.6. Mössbauer Spectroscopy

The significant difference in isomer shift between ferrous and ferric iron make Mössbauer spectroscopy a useful technique to determine iron oxidation state. In general, a Mössbauer spectrum will display a quadrupole doublet for each type of coordination environment. The center of the two lines, the isomer shift, is dependent on various factors of which oxidation state and coordination geometry are most important in clays. In addition to the isomer shift, information about the

825 electric field gradient can be gleaned from the quadrupole splitting (ΔE_Q), which can
826 be used to distinguish different coordination environments.
827
828 Mössbauer data were collected on 11 out of 16 species (Figure 11). Data
829 collection of samples G-J and P was hampered by the low concentrations of iron,
830 especially because samples were not synthesized using ^{57}Fe doped material. The
831 Mössbauer spectra collected for samples A-F show either an unresolved quadrupole
832 doublet or quadrupole doublets with a small quadrupole splitting (Figure 11a). The
833 small quadrupole splitting for these samples is characteristic of high-spin Fe(III) in
834 an octahedral coordination environment. Although the spectra of A-F are broad,
835 they can be fit well with a single quadrupole doublet with isomer shifts between
836 0.34 and 0.36 mm s^{-1} (Table 5). These isomer shifts are characteristic of octahedral
837 Fe(III) sites (Burns, 1994) and within the range of Fe(III) smectites (0.33-0.37 mm s^{-1})
838 (Murad and Schwertmann 1984; Treiman et al. 2014). No ferrous material is
839 present based on the absence of quadrupole doublets with an isomer shift above 1.0
840 mm s^{-1} (Chemtob et al. 2015). For sample A, an improved fit was obtained with a
841 small tetrahedral site Fe component (7.5%), resulting in an isomer shift of 0.25 and
842 quadrupole splitting of 1.50, but the large overlap between peaks also produced
843 high uncertainty.
844
845 The Mössbauer spectra collected for K-O show a quadrupole doublet centered
846 between 1.10 and 1.15 mm s^{-1} characteristic for octahedral Fe(II) and a smaller
847 broad unresolved quadrupole doublet due to Fe(III) (Figure 10b, Table 5). Most

848 spectra of K-O can be fit with well with a single quadrupole doublet with linewidths
849 between 0.4-0.5 mm s^{-1}. The high isomer shifts observed (>1 mm s^{-1}) are
850 characteristic of octahedral Fe(II) sites and are comparable to those observed for
851 similar Fe(II) smectites (Chemtob et al. 2015). Although the spectra recorded by our
852 other techniques show distinct difference upon changing the iron ratio, the
853 quadrupole splitting and isomer shifts (Table 5, and Figure 10c, 10d) do not show
854 any consistent variation with increasing or decreasing Fe content. The absence of
855 any systematic variation with Fe content is consistent with Mössbauer observations
856 made for the jarosite family (McCollom et al. 2014) and for Fe(II) smectites by
857 Chemtob *et al* 2015.
858
859 Fitting the areas of the doublets yields Fe(II)/Fe(III) ratios in close agreement
860 with those determined by other techniques (Table 5). The ratios of samples K and L
861 deviate more, which is likely due to oxidation during storage or the handling
862 process of these samples. The Fe(II) ratio measured in sample K decreased between
863 subsequent measurements before and after the sample was handled in air (Figure
864 S1). Due to the oxidation, the ratios only represent a lower bound on the Fe(II)
865 content at the time of synthesis.
866
867 As Mössbauer spectra of Fe phases typically have temperature dependent effects
868 and the temperature of sample measurement can vary under planetary conditions,
869 we investigated the temperature dependency on the isomer shift two samples,
870 Fe(III)-bearing sample A and Fe(II)-bearing K. Spectra were recorded between 80 and

320 K (Figure 12). In line with work on octahedral Fe(III) by *e.g.* DeGraven and Alboom (1991),the isomer shift of both samples exhibits a dramatic decrease of 0.14 mm s^{-1} upon cooling the samples from 320 to 80K (Table 6). The difference of 0.1 mm s^{-1} between 293 K and 80 K is the same that observed for certain nontronites (Murad et al. 1987). No additional hyperfine features were resolved at lower temperatures and therefore the other samples were collected at room temperature, which is also consistent with previous studies (Chemtob et al., 2015, McCollom et al., 2014, Morris et al., 2006).

4. Implications for planetary remote sensing and in-situ exploration

This study demonstrates the synergies and limits of multiple measurement types for the detection of smectite chemistry and oxidation state on planetary surfaces to infer past geochemical conditions. Reflectance spectroscopy has previously been shown to detect alteration minerals, including smectite clays, at levels ~10% in natural mineral assemblages (Ehlmann et al. 2012; Greenberger et al. 2012). We demonstrate that smectite composition and the dominant oxidation state of Fe in the octahedral state can be identified in the near infrared on the basis of their metal-OH vibrational modes. The 2.0-3μm region is particularly useful. The fundamental M-OH stretching modes between 2.6-2.9μm vary systematically with chemistry, and the metal-OH minimum wavelength increases for smectites with Mg, Al, Fe(II) and Fe(III) respectively. Smectites dominated by Mg or Fe(III) are spectrally distinct, whereas Al-rich and Fe(II) rich smectites both have minima near 2.76 (Figure 7). This absorption has been interpreted to represent Al phyllosilicates in Ceres bright

894 spots (De Sanctis et al. 2016), but our study shows that the spectral pattern would
895 also be consistent with the presence of Fe(II) smectites. Use of multiple wavelength
896 regions in the NIR can yield unique solutions, if overtone and combination
897 absorptions are present in remotely sensed data. The ~2.24 μm absorption tracks
898 Mg substitution well, and the M-OH feature near 2.32 is diagnostic of Fe(III) vs.
899 Fe(II), shifting considerably with Mg substitution in Fe(II) smectites only (Figure 5).
900 This multiple wavelength approach extends previous analyses of the 2.3 μm's
901 variation with octahedral sheet occupancy and iron content (Michalski et al., 2015).
902 The overtone and fundamental H_2O stretches at 1.9 and 3μm provide additional
903 information on the degree of hydration in smectites. The visible wavelength region
904 can provide qualitative auxiliary information about Fe oxidation, but the electronic
905 absorptions observed between 0.4-1 μm are not unique to smectite clays, so the M-
906 OH features are more diagnostic of smectite speciation, particularly in mineral
907 assemblages.
908
909 As instrument builders consider implementation approaches, spatial and spectral
910 resolution, as well as signal-to-noise (SNR), are key considerations to enable
911 discrimination of the diagnostic absorptions. Many NIR reflectance spectrometers,
912 such as the Mars Express/OMEGA, MRO/CRISM, Dawn/VIR, Osiris-Rex/OVIRS and
913 Cassini/VIMS, are sensitive from ~1-4/5μm with sufficient spectral resolution to
914 distinguish the features discussed above, and provide global views of planetary
915 surfaces at relatively large pixel footprints between tens and hundreds of meters
916 square. Higher spatial resolution, of course, allows mineral identifications to be

917 better associated with particular strata or geomorphic features, improving geologic
918 interpretations and providing further constraints on alteration environments.
919 Detailed analysis of spectral variation on the hand-sample scale (mm-cm) is
920 particularly useful to identify alteration textures and spatial patterns, all of which
921 provide key context in understanding the alteration environment. Such fine
922 resolution VNIR spectral analysis will be employed for the first time on Mars
923 onboard the Mars-2020 rover by the SuperCam instrument (Wiens et al. 2017) and
924 on the Exo-Mars rover by Ma_MISS (De Sanctis et al. 2017) and micrOmega (Bibring
925 et al. 2017).
926
927 In the mid-infrared, the silicate stretching and bending modes active in smectite
928 clays are common to other silicates as well, and the M-OH bending modes are
929 discernable but overlap and combine, making direct identification of a particular
930 smectite species challenging, particularly if the measurement is of a bulk mineral
931 assemblage. Michalski et al. (2005) demonstrated how the Si-O and M-O bends
932 changed in character between dioctahedral and trioctahedral smectites. Here we
933 demonstrate that the 450 cm^{-1} absorption systematically varies in position with
934 octahedral Fe(III) and Fe(II) content, although other information from the VNIR (or
935 Mössbauer in-situ) must be brought to bear to determine the oxidation state and the
936 the relationship between absorption position and Fe content (Figure 8b). The Mars
937 Global Surveyor Thermal Emission Spectrometer (TES) and Mars Exploration Rover
938 Mini-TES thermal emission instruments in orbit around and on the surface of Mars,
939 respectively, have been used with this multi-instrument approach to conduct

940 surveys with other orbiting or payload elements specifically characterizing smectite
941 minerals and alteration phases (Michalski et al. 2006, 2010; Ruff and Christensen
942 2007). OTES on Osiris-REX, along with OVIRS, is also characterizing the
943 phyllosilicates on the asteroid Bennu (Hamilton et al., 2019). With our expanded
944 spectral libraries, more refined characterization of smectites from MIR data is now
945 possible.
946
947 Raman spectroscopy is a new addition to planetary science instrumentation, and
948 is opening new avenues for in-situ remote mineralogical analysis of planetary
949 surfaces, as well as the detection of organic components. The green Raman
950 SuperCam Raman system is designed to obtain patterns from several meters distant
951 to the target from on the mast of the Mars 2020 rover (Wiens et al. 2017), and the
952 deep-UV Raman SHERLOC system will interrogate rock surfaces on the micrometer
953 scale from its position on the Mars 2020 rover arm (Beegle et al. 2017). Our data
954 provides the first Raman spectral libraries as a function of their chemistry (Figure 9,
955 10). Precise identification of smectite clays, and clay minerals in general, will likely
956 be a challenge in natural mineral assemblages due to the generally low Raman
957 intensities inherent to clay minerals and sensitivity to complex lattice variation.
958 However, the M-OH stretching modes between 3000-4000cm^{-1} in both Green and
959 Deep UV Raman data sets will useful for identifying phyllosilicates and qualitatively
960 judging their composition. In both Raman excitation modes, it is possible in some
961 cases to detect the Fe(III), Al, and Mg-OH stretching modes, although intensity
962 decreases significantly as Fe content increases. The M-OH bending modes and

963 silicate features between 400-1000cm^{-1} require high signal to noise to be
964 distinguished, and are likely to be overlapping with more crystalline phases in
965 natural mineral assemblages that would mask phyllosilicate detection.
966 Photoluminescence, which is frequently much stronger than Raman signal, is also a
967 likely obstacle in identifying mineral assemblages on planetary surfaces; Fe(II)
968 bearing smectites are apparently more susceptible to photoluminescence when
969 using a 532nm excitation laser than DUV (Figure 10). Carrying more than one
970 excitation laser, as the Mars 2020 rover is planning, may help mitigate
971 photoluminescence concerns, as switching wavelengths can reduce the effect for a
972 given material. Thus, Raman is best used in concert with other approaches for
973 characterization smectite-bearing mineral assemblages.
974
975 In-situ XRD analyses offer the most quantitative means to measure the absolute
976 abundance of smectite clays and their coordination (Figure 3). The Chemistry and
977 Mineralogy Analyzer instrument (CheMin), an X-Ray diffractometer onboard the
978 Mars Science Laboratory rover Curiosity, has demonstrated the common occurrence
979 of smectite clays in the sedimentary deposits within Gale Crater (Vaniman et al.
980 2013; Bristow et al. 2018). Notably, our sample set of synthetic smectites have peak
981 positions, as corrected for measurements using Co Ka radiation (Table 2), that cover
982 the full range of observations of martian smectites in Gale crater (Vaniman et al.
983 2013; Treiman et al. 2014; Bristow et al. 2018). This demonstrates that, potentially,
984 the compositions of the data set presented here is representative of the martian
985 samples, and that all martian observations can be consistent with the presence of a

single smectite, and that mixtures of dioctahedral and trioctahedral phases are not required to describe the features observed (e.g., Bristow et al., 2018). The CheMin instrument requires the use of the position of the (02,11) peak to calculate the octahedral site occupancy of smectites measured in Gale Crater, Mars, as the (06,33) peak occurs outside the diffraction range. Our results demonstrate that it is critical to recognize that peak positions of the (02,11) bands produce substantial systematic errors if used to obtain lattice parameters of smectites. Use of the (06,33) band peak positions, widely employed in terrestrial studies of clays but inaccessible by the ChemMin instrument on MSL, yields an order of magnitude smaller systematic error. Thus, as with prior investigations, our study shows the value of incorporating the (06,33) peak into instrument diffraction ranges in order to best distinguish dioctahedral and trioctahedral smectites. In most laboratory settings, clay mineral fractions are separated from the rest of the sample, making measurements more straightforward, but martian samples are measured in bulk, which can further obfuscate precise analysis and calculation of lattice parameters. Consequently, identifications of specific phyllosilicate phases are most easily made when applying secondary information. On the Curiosity rover, this is water release temperature from Evolved Gas Analysis with the SAM instrument (Bristow et al. 2015). VNIR, MIR and Mössbauer are also highly synergistic because they provide information on the Fe oxidation state that XRD alone cannot.

Mössbauer spectra can aid in confirming detections of smectite minerals using the measured isomer shifts and patterns in quadrupole splittings. Particularly,

Mössbauer measurements provide a quantitative and highly sensitive means to determine Fe(II)/Fe(III) ratios better all other analysis techniques discussed here, but do not demonstrate uniquely identifying patterns that distinguish smectites of varying quantitative Fe content from one another. Consequently, Mössbauer spectroscopy is best utilized in conjunction with other in-situ approaches to examine alteration mineralogy. The Mössbauer parameters reported here, derived from room temperature measurements, can be used in direct comparison to extra-terrestrial Mössbauer measurements, despite overall ambient temperature differences between the library and in-situ measurements (Morris et. al., 2006). The temperature dependence derives from the temperature gradient between the sample and source, which while highlighting hyperfine structures, renders comparisons to measurements under different temperature gradient conditions ill-posed. However, Mössbauer measurements made in extra-terrestrial settings, such as by the Mars Exploration Rovers, have kept both the source and samples (planetary surfaces) at the same ambient temperature. Our measurements also have a negligible temperature difference between source and sample measured at room temperature, so we thus mitigate the temperature dependencies of the derived parameters, creating a database for application to determination of smectite presence and Fe.

Collectively, the data presented here are foundational for the study of smectite clays across the solar system. The ability to determine the coordination, crystal chemistry,

and oxidation state will enable new insights into the geological and environmental evolution of planetary bodies.

5. Acknowledgements

This work was funded by a NASA Solar Systems Workings grant (NNX15AH53G) to B.L.E. Thanks to George Rossman for the use of his ATR and Raman instruments, as well as sage advice. Thanks also to Rohit Bhartia for use of the DUV Raman system. We also thank our reviewers, Benoit Dubacq and Jebril Hadi, for extremely thoughtful reviews that greatly improved the quality of our manuscript.

6. References

*References noted by [#] are source materials of data in Figure 1.

Abbey, W.J., Bhartia, R., Beegle, L.W., DeFlores, L., Paez, V., Sijapati, K., Sijapati, S., Williford, K., Tuite, M., Hug, W., and others (2017) Deep UV Raman spectroscopy for planetary exploration: The search for in situ organics. Icarus, 290, 201–214.

Ammannito, E., DeSanctis, M.C., Ciarniello, M., Frigeri, A., Carrozzo, F.G., Combe, J.-P., Ehlmann, B.L., Marchi, S., McSween, H.Y., Raponi, A., and others (2016) Distribution of phyllosilicates on the surface of Ceres. Science, 353, aaf4279.

1052 Andrieux, P., and Petit, S. (2010) Hydrothermal synthesis of dioctahedral smectites:
1053 The Al–Fe3+ chemical series: Part I: Influence of experimental conditions.
1054 Applied Clay Science, 48, 5–17.

1055 [1] April, R.H., and Keller, D.M. (1992) Saponite and vermiculite in amygdales of the
1056 Granby Basaltic Tuff, Connecticut Valley. Clays and Clay Minerals, 40, 22-31.

1057 Arvidson, R.E., Squyres, S.W., Bell, J.F., Catalano, J.G., Clark, B.C., Crumpler, L.S., de
1058 Souza, P.A., Fairén, A.G., Farrand, W.H., Fox, V.K., and others (2014) Ancient
1059 Aqueous Environments at Endeavour Crater, Mars. Science, 343.

1060 Asher, S.A., and Johnson, C.R. (1984) Raman spectroscopy of a coal liquid shows that
1061 fluorescence interference is minimized with ultraviolet excitation. Science,
1062 225, 311–313.

1063 Badaut, D., Besson, G., Decarreau, A., and Rautureau, R. (1985) Occurrence of a
1064 ferrous, trioctahedral smectite in Recent sediments of Atlantis II Deep, Red
1065 Sea. Clay Minerals, 20, 389–404.

1066 Beegle, L., Bhartia, R., White, M., DeFlores, L., Abbey, W., Wu, Y.-H., Cameron, B.,
1067 Moore, J., Fries, M., Burton, A., and others (2015) SHERLOC: Scanning
1068 habitable environments with Raman amp; luminescence for organics amp;
1069 chemicals. In 2015 IEEE Aerospace Conference pp. 1–11. Presented at the
1070 2015 IEEE Aerospace Conference.

1071 Beegle, L.W., Bhartia, R., Carrier, B., DeFlores, L., Abbey, W., Asher, S., Burton, A.,
1072 Fries, M., Conrad, P., Clegg, S., and others (2017) The SHERLOC Investigation.
1073 Lunar and Planetary Science Conference, 2839.

1074 Bergmann, J., Friedel, P., and Kleeberg, R. (1998) BGMN - a new fundamental
1075 parameters based Rietveld program for laboratory X-ray sources, it's use in
1076 quantitative analysis and structure investigations. Commission on Powder
1077 Diffraction (IUCr) Newsletter, 20, 5–8.

1078 [2] Besson, G., and Tchoubar, C. (1972) Détermination du groupe de symétrie du
1079 feuillet élémentaire de la beidellite. Comptes Rendus Hebdomadaires des
1080 Séances de l'Académie Des Sciences Serie D, 275, 633-636.

1081 Bibring, J.-P., Langevin, Y., Mustard, J.F., Poulet, F., Arvidson, R., Gendrin, A., Gondet,
1082 B., Mangold, N., Pinet, P., Forget, F., and others (2006) Global Mineralogical
1083 and Aqueous Mars History Derived from OMEGA/Mars Express Data. Science,
1084 312, 400–404.

1085 Bibring, J.-P., Hamm, V., Pilorget, C., Vago, J.L., and the MicrOmega Team (2017) The
1086 MicrOmega Investigation Onboard ExoMars. Astrobiology, 17, 621–626.

1087 Bishop, J. L., and Murad (2004) Characterization of minerals and biogeochemical
1088 markers on Mars: A Raman and IR spectroscopic study of montmorillonite.
1089 Journal of Raman Spectroscopy, 35, 480–486.

1090 Bishop, J.L., Pieters, C.M., and Edwards, J.O. (1994) Infrared Spectroscopic Analyses
1091 on the Nature of Water in Montmorillonite. Clays and Clay Minerals, 42, 702–
1092 716.

1093 Bishop, J. L., Dobrea, E.Z.N., McKeown, N.K., Parente, M., Ehlmann, B.L., Michalski, J.R.,
1094 Milliken, R.E., Poulet, F., Swayze, G.A., Mustard, J.F., and others (2008a)
1095 Phyllosilicate Diversity and Past Aqueous Activity Revealed at Mawrth Vallis,
1096 Mars. Science, 321, 830–833.

1097 Bishop, J.L., Lane, M.D., Dyar, M.D., and Brown, A.J. (2008b) Reflectance and emission
1098 spectroscopy study of four groups of phyllosilicates: smectites, kaolinite-
1099 serpentines, chlorites and micas. Clay Minerals, 43, 35–54.

1100 Bishop, J. L., Lane, M.D., Dyar, M.D., and Brown, A.J. (2008c) Reflectance and
1101 emission spectroscopy study of four groups of phyllosilicates: smectites,
1102 kaolinite-serpentines, chlorites and micas. Clay Minerals, 43, 35–54.

1103 Brindley, G.W., and Brown, G. (1980) Crystal structures of clay minerals of clay
1104 minerals and their X-ray identification. Mineralogical Society Monograph.

1105 Bristow, T.F., Bish, D.L., Vaniman, D.T., Morris, R.V., Blake, D.F., Grotzinger, J.P.,
1106 Rampe, E.B., Crisp, J.A., Achilles, C.N., Ming, D.W., and others (2015) The
1107 origin and implications of clay minerals from Yellowknife Bay, Gale crater,
1108 Mars. American Mineralogist, 100, 824–836.

1109 Bristow, T.F., Rampe, E.B., Achilles, C.N., Blake, D.F., Chipera, S.J., Craig, P., Crisp, J.A.,
1110 Marais, D.J.D., Downs, R.T., Gellert, R., and others (2018) Clay mineral
1111 diversity and abundance in sedimentary rocks of Gale crater, Mars. Science
1112 Advances, 4, eaar3330.

1113 Bunch, T.E., and Chang, S. (1980) Carbonaceous chondrites—II. Carbonaceous
1114 chondrite phyllosilicates and light element geochemistry as indicators of
1115 parent body processes and surface conditions. Geochimica et Cosmochimica
1116 Acta, 44, 1543–1577.

1117 Burns, R.G. (1970) Crystal field spectra and evidence of cation ordering in olivine
1118 minerals. American Mineralogist, 55, 1608–1632.

1119 Burns, R.G. (1993) Rates and mechanisms of chemical weathering of ferromagnesian
1120 silicate minerals on Mars. Geochimica et Cosmochimica Acta, 57, 4555–4574.

1121 Carter, J., Poulet, F., Bibring, J.-P., Mangold, N., and Murchie, S. (2013) Hydrous
1122 minerals on Mars as seen by the CRISM and OMEGA imaging spectrometers:
1123 Updated global view. Journal of Geophysical Research: Planets, 118, 831–858.

1124 [3] Castellini, E., Malferrari, D., Bernini, F., Brigatti, M.F., Castro, G.R., Medici, L.,
1125 Mucci, A., and Borsari, M. (2017) Baseline Studies of the Clay Minerals Society
1126 Source Clay Montmorillonite STx-1b. Clays and Clay Minerals, 65, 220-233.

1127 Catalano, J.G. (2013) Thermodynamic and mass balance constraints on iron-bearing
1128 phyllosilicate formation and alteration pathways on early Mars. Journal of
1129 Geophysical Research: Planets, 118, 2124–2136.

1130 Catling, D.C., and Moore, J.M. (2003) The nature of coarse-grained crystalline
1131 hematite and its implications for the early environment of Mars. Icarus, 165,
1132 277–300.

1133 Chemtob, S.M., Nickerson, R.D., Morris, R. V, Agresti, D.G., and Catalano, J.G. (2015)
1134 Synthesis and structural characterization of ferrous trioctahedral smectites:
1135 Implications for clay mineral genesis and detectability on Mars. Journal of
1136 Geophysical Research: Planets, 120, 1119–1140.

1137 Chemtob, S.M., Nickerson, R.D., Morris, R. V, Agresti, D.G., and Catalano, J.G. (2017)
1138 Oxidative alteration of ferrous smectites and implications for the redox
1139 evolution of early Mars. Journal of Geophysical Research: Planets,
1140 2017JE005331.

1141 Clark, R.N., King, T.V.V., Klejwa, M., Swayze, G.A., and Vergo, N. (1990) High spectral
1142 resolution reflectance spectroscopy of minerals. Journal of Geophysical
1143 Research: Solid Earth, 95, 12653–12680.

1144 [4] Curtis, C.D. (1976) Unmixed Ca^{2+}-Mg^{2+} saponite at Calton Hill, Derbyshire. Clay
1145 Minerals, 11, 85-89.

[5] Daynyak, L.G., Drits, V.A., Kudryavtsev, D.I., Simanovich, I.M., and Slonimskaya, M.V. (1981) Crystal chemical specificity of trioctahedral smectites: Products of secondary alteration of oceanic and continental basalts. Doklady Akademii Nauk SSSR, 259, 1458-1462.

De Sanctis, M.C., Ammannito, E., Raponi, A., Marchi, S., McCord, T.B., McSween, H.Y., Capaccioni, F., Capria, M.T., Carrozzo, F.G., Ciarniello, M., and others (2015) Ammoniated phyllosilicates with a likely outer Solar System origin on (1) Ceres. Nature, 528, 241–244.

De Sanctis, M.C., Altieri, F., Ammannito, E., Biondi, D., De Angelis, S., Meini, M., Mondello, G., Novi, S., Paolinetti, R., Soldani, M., and others (2017) Ma_MISS on ExoMars: Mineralogical Characterization of the Martian Subsurface. Astrobiology, 17, 612–620.

[6] Desprairies, A., Tremblay, P., and Laloy, C. (1989) Secondary Mineral Assemblages in a Volcanic Sequence Drilled during ODP Leg 104 in the Norwegian Sea. Proceedings of the Ocean Drilling Program, Scientific Results, 104, 397-409.

Decarreau, A., and Bonnin, D. (1986) Synthesis and crystallogenesis at low temperature of Fe(III)-smectites by evolution of coprecipitated gels: experiments in partially reducing conditions. Clay Minerals, 21, 861–877.

1165 Decarreau, A., Petit, S., Martin, F., Farges, F., Vieillard, P., and Joussein, E. (2008)
1166 Hydrothermal synthesis, between 75 and 150°C, of high-charge, ferric
1167 nontronites. Clays and Clay Minerals, 56, 322–337.

1168 de Ligny, D., Guillaud, E., Gailhanou, H., & Blanc, P. (2013). Raman Spectroscopy of
1169 Adsorbed Water in Clays: First Attempt at Band Assignment. *Procedia Earth and*
1170 *Planetary Science*, *7*, 203–206.

1171 Doebelin, N., and Kleeberg, R. (2015) Profex: a graphical user interface for the
1172 Rietveld refinement program BGMN. Journal of Applied Crystallography, 48,
1173 1573–1580.

1174 Ehlmann, B.L., and Edwards, C.S. (2014) Mineralogy of the Martian Surface. Annual
1175 Review of Earth and Planetary Sciences, 42, 291–315.

1176 Ehlmann, B.L., Mustard, J.F., Murchie, S.L., Bibring, J.-P., Meunier, A., Fraeman, A.A.,
1177 and Langevin, Y. (2011) Subsurface water and clay mineral formation during
1178 the early history of Mars. Nature, 479, 53–60.

1179 Ehlmann, B.L., Bish, D.L., Ruff, S.W., and Mustard, J.F. (2012) Mineralogy and
1180 chemistry of altered Icelandic basalts: Application to clay mineral detection
1181 and understanding aqueous environments on Mars. Journal of Geophysical
1182 Research: Planets, 117, E00J16.

1183 Ferrari, A.C., and Robertson, J. (2001) Resonant Raman spectroscopy of disordered,
1184 amorphous, and diamondlike carbon. Physical Review B, 64, 075414.

1185 Fox, V.K., Arvidson, R.E., Guinness, E.A., McLennan, S.M., Catalano, J.G., Murchie, S.L.,
1186 and Powell, K.E. (2016) Smectite deposits in Marathon Valley, Endeavour
1187 Crater, Mars, identified using CRISM hyperspectral reflectance data.
1188 Geophysical Research Letters, 43, 2016GL069108.

1189 Frost, R.L., and Kloprogge, J.T. (2000a) Raman Spectroscopy of Nontronites. Applied
1190 Spectroscopy, 54, 402–405.

1191 Frost, R.L, and Kloprogge, J.T. (2000b) Vibrational spectroscopy of ferruginous
1192 smectite and nontronite. Spectrochimica Acta Part A: Molecular and
1193 Biomolecular Spectroscopy, 56, 2177–2189.

1194 [7] Gailhanou, H., Blanc, P., Rogez, J., Mikaelian, G., Kawaji, H., Olives, J., Amouric, M.,
1195 Denoyel, R., Bourrelly, S., Montouillout, V., Vieillard, P., Fialips, C.I., Michau, N.,
1196 and Gaucher, E.C. (2012) Thermodynamic properties of illite, smectite and
1197 beidellite by calorimetric methods: Enthalpies of formation, heat capacities,
1198 entropies and Gibbs free energies of formation. Geochimica et Cosmochimica
1199 Acta, 89, 279-301.

1200 Gainey, S.R., Hausrath, E.M., Adcock, C.T., Tschauner, O., Hurowitz, J.A., Ehlmann, B.L.,
1201 Xiao, Y., and Bartlett, C.L. (2017) Clay mineral formation under oxidized
1202 conditions and implications for paleoenvironments and organic preservation
1203 on Mars. Nature Communications, 8, 1–7.

1204 [8]Gates, W.P. (2005) Infrared spectroscopy and the chemistry of dioctahedral
1205 smectites. In J.T. Kloprogge, Ed., CMS Workshop Lectures Vol. 13. Clay
1206 Minerals Society.

1207 Gates, W.P., Petit, S., and Madejová, J. (2017) Chapter 7 - Applications of NIR/MIR to
1208 Determine Site Occupancy in Smectites. In W.P. Gates, J.T. Kloprogge, J.
1209 Madejová, and F. Bergaya, Eds., Developments in Clay Science Vol. 8, pp. 200–
1210 221. Elsevier.

1211 [9] Gaudin, A., Petit, S., Rose, J., Martin, F., Decarreau, A., Noack, Y., and Borschneck,
1212 D. (2004) The accurate crystal chemistry of ferric smectites from the lateritic
1213 nickel ore of Murrin Murrin (Western Australia). II. Spectroscopic (IR and
1214 EXAFS) approaches. Clay Minerals, 39, 453-467.

1215 Grauby, O., Petit, S., Decarreau, A., and Baronnet, A. (1993) The beidellite-saponite
1216 series: an experimental approach. European Journal of Mineralogy, 623–636.

1217 Grauby, O., Petit, S., Decarreau, A., and Baronnet, A. (1994) The nontronite-saponite
1218 series: An experimental approach. European Journal of Mineralogy, 99–112.

1219 Greenberger, R.N., Mustard, J.F., Kumar, P.S., Dyar, M.D., Breves, E.A., and Sklute, E.C.
1220 (2012) Low temperature aqueous alteration of basalt: Mineral assemblages
1221 of Deccan basalts and implications for Mars. Journal of Geophysical Research:
1222 Planets, 117, E00J12.

1223 Grotzinger, J.P., Sumner, D.Y., Kah, L.C., Stack, K., Gupta, S., Edgar, L., Rubin, D., Lewis,
1224 K., Schieber, J., Mangold, N., and others (2014) A Habitable Fluvio-Lacustrine
1225 Environment at Yellowknife Bay, Gale Crater, Mars. Science, 343.

1226 Guven, N. (1988) Smectites. Reviews in Mineralogy and Geochemistry, 19, 497–559.

1227 Hunt, G. (1977) Spectral signatures of particulate minerals in the visible and near
1228 infrared. GEOPHYSICS, 42, 501–513.

1229 [10] Inoue, A., and Utada, M. (1991) Smectite-to-chlorite transformation in
1230 thermally metamorphosed volcanoclastic rocks in the Kamikita area,
1231 northern Honshu, Japan. American Mineralogist, 76, 628-640.

1232 Keeling, J.L., Raven, M.D., and Gates, W.P. (2000) Geology and characterization of
1233 two hydrothermal nontronites from weathered metamorphic rocks at the
1234 Uley graphite mine, South Australia. Clays and Clay Minerals, 48, 537–548.

1235 [11] Kimbara, K., and Honda, S. (1975) An iron-rich saponite-like mineral found in
1236 the Moriyama volcanic rocks, Gojome, Akita Prefecture, Japan. Bull. Geol.
1237 Surv. Japan, 26, 37-40.

1238 [12] Kodama, H., Dekimpe, C.R., and Dejou, J. (1988) Ferrian saponite in a gabbro
1239 saprolite at Mont Mégantic, Quebec. Clays and Clay Minerals, 36, 102-110.

1240 Kohyama, N., Shimoda, S., and Sudo, T. (1973) Iron-rich saponite (ferrous and ferric
1241 forms). Clays and Clay Minerals, 21, 229-237.

1242 Kohyama, N., Shimoda, S., and Sudo, T. (1973) Iron-Rich Saponite (Ferrous and
1243 Ferric Forms). Clays and Clay Minerals, 21, 229–237.

1244 [13] Koster, H.M., Ehrlicher, U., Gilg, H.A., Jordan, R., Murad, E., and Onnich, K. (1999)
1245 Mineralogical and chemical characteristics of five nontronites and Fe-rich
1246 smectites. Clay Minerals, 34, 579-599.

1247 Lajarige, C., Petit, S., Augas, C., and Decarreau, A. (1998) Stabilisation of Fe2+ ions in
1248 synthetic ferroan smectites. Comptes Rendus de l'Academie des Sciences
1249 Series IIA Earth and Planetary Science, 12, 789–794.

1250 Madejová, J., and Pálková, H. (2017) Chapter 13 - NIR Contribution to The Study of
1251 Modified Clay Minerals. In W.P. Gates, J.T. Kloprogge, J. Madejová, and F.
1252 Bergaya, Eds., Developments in Clay Science Vol. 8, pp. 447–481. Elsevier.

1253 Madejová, J., Komadel, P., and Číčel, B. (1994) Infrared study of octahedral site
1254 populations in smectites. Clay Minerals, 29, 319–326.

1255 Madejová, J., Bujdák, J., Petit, S., and Komadel, P. (2000) Effects of chemical
1256 composition and temperature of heating on the infrared spectra of Li-
1257 saturated dioctahedral smectites. (II) Near- infrared region. Clay Minerals,
1258 35, 753–761.

1259 Madejová, J., Janek, M., Komadel, P., Herbert, H.-J., and Moog, H.C. (2002) FTIR
1260 analyses of water in MX-80 bentonite compacted from high salinary salt
1261 solution systems. Applied Clay Science, 20, 255–271.

McCollom, T.M., Ehlmann, B.L., Wang, A., Hynek, B.M., Moskowitz, B., and Berquó, T.S. (2014) Detection of iron substitution in natroalunite-natrojarosite solid solutions and potential implications for Mars. American Mineralogist, 99, 948–964.

[14] Mermut, A.R., and Cano, A.F. (2001) Baseline studies of The Clay Minerals Society Source Clays: Chemical analyses of major elements. Clays and Clay Minerals, 49, 381-386.

Michalski, J., Poulet, F., Bibring, J.-P., and Mangold, N. (2010) Analysis of phyllosilicate deposits in the Nili Fossae region of Mars: Comparison of TES and OMEGA data. Icarus, 206, 269–289.

Michalski, J.R., Kraft, M.D., Sharp, T.G., Williams, L.B., and Christensen, P.R. (2006) Emission spectroscopy of clay minerals and evidence for poorly crystalline aluminosilicates on Mars from Thermal Emission Spectrometer data. Journal of Geophysical Research: Planets, 111, E03004.

Michalski, J.R., Cuadros, J., Bishop, J.L., Darby Dyar, M., Dekov, V., and Fiore, S. (2015) Constraints on the crystal-chemistry of Fe/Mg-rich smectitic clays on Mars and links to global alteration trends. Earth and Planetary Science Letters, 427, 215–225.

Moore, D.M., and Reynolds, R.C. (1997) X-Ray Diffraction and the Identification and Analysis of Clay Minerals. Oxford University Press, New York.

1282 Morgan, J., and Warren, B.E. (1938) X-Ray Analysis of the Structure of Water. The
1283 Journal of Chemical Physics, 6, 666–673.

1284 Morris, R. V., Klingelhöfer, G., Schröder, C., Rodionov, D. S., Yen, A., Ming, D. W.,
1285 Souza, P. A. de, Fleischer, I., Wdowiak, T., Gellert, R., Bernhardt, B., Evlanov, E.
1286 N., Zubkov, B., Foh, J., Bonnes, U., Kankeleit, E., Gütlich, P., Renz, F., Squyres, S.
1287 W., & Arvidson, R. E. (2006). Mössbauer mineralogy of rock, soil, and dust at
1288 Gusev crater, Mars: Spirit's journey through weakly altered olivine basalt on
1289 the plains and pervasively altered basalt in the Columbia Hills. *Journal of*
1290 *Geophysical Research: Planets*, *111*(E2).
1291 https://doi.org/10.1029/2005JE002584

1292 Murad, E., and Schwertmann, U. (1984) The influence of crystallinity on the
1293 Mössbauer spectrum of lepidocrocite. Mineralogical Magazine, 48, 507–511.

1294 [15] Niu, B., and Yoshimura, T. (1996) Smectite conversion in diagenesis and low
1295 grade hydrothermal alteration from Neogene basaltic marine sediments in
1296 Niigata Basin, Japan. Clay science, 10, 37-56.

1297 [16] Parthasarathy, G., Choudary, B.M., Sreedhar, B., Kunwar, A.C., and Srinivasan, R.
1298 (2003) Ferrous saponite from the Deccan Trap, India, and its application in
1299 adsorption and reduction of hexavalent chromium. American Mineralogist,
1300 88, 1983-1988.

1301 Petit, S., Decarreau, A., Gates, W., Andrieux, P., and Grauby, O. (2015) Hydrothermal
1302 synthesis of dioctahedral smectites: The Al–Fe3+ chemical series. Part II:
1303 Crystal-chemistry. Applied Clay Science, 104, 96–105.

1304 [17] Post, J.L. (1984) Saponite from near Ballarat, California. Clays and Clay
1305 Minerals, 32, 147-153.

1306 Poulet, F., Bibring, J.-P., Mustard, J.F., Gendrin, A., Mangold, N., Langevin, Y., Arvidson,
1307 R.E., Gondet, B., Gomez, C., Berthé, M., and others (2005) Phyllosilicates on
1308 Mars and implications for early martian climate. Nature, 438, 623–627.

1309 Poulet, F., Mangold, N., Loizeau, D., Bibring, J.-P., Langevin, Y., Michalski, J., and
1310 Gondet, B. (2008) Abundance of minerals in the phyllosilicate-rich units on
1311 Mars. Astronomy and Astrophysics, 487, L41–L44.

1312 Quirico, E., Montagnac, G., Rouzaud, J.-N., Bonal, L., Bourot-Denise, M., Duber, S., and
1313 Reynard, B. (2009) Precursor and metamorphic condition effects on Raman
1314 spectra of poorly ordered carbonaceous matter in chondrites and coals.
1315 Earth and Planetary Science Letters, 287, 185–193.

1316 Rampe, E.B., Ming, D.W., Blake, D.F., Bristow, T.F., Chipera, S.J., Grotzinger, J.P.,
1317 Morris, R.V., Morrison, S.M., Vaniman, D.T., Yen, A.S., and others (2017)
1318 Mineralogy of an ancient lacustrine mudstone succession from the Murray
1319 formation, Gale crater, Mars. Earth and Planetary Science Letters, 471, 172–
1320 185.

1321 Rivkin, A.S., Davies, J.K., Johnson, J.R., Ellison, S.L., Trilling, D.E., Brown, R.H., and
1322 Lebofsky, L.A. (2003) Hydrogen concentrations on C-class asteroids derived
1323 from remote sensing. Meteoritics & Planetary Science, 38, 1383–1398.

1324 Rivkin, A.S., Volquardsen, E.L., and Clark, B.E. (2006) The surface composition of
1325 Ceres: Discovery of carbonates and iron-rich clays. Icarus, 185, 563–567.

1326 Rossman, G.R. (1976) Spectroscopic and magnetic studies of ferric iron hydroxy
1327 sulfates: the series Fe(OH)SO_4·nH_2O and the jarosites. American
1328 Mineralogist, 61, 398–404.

1329 Ruff, S.W., and Christensen, P.R. (2007) Basaltic andesite, altered basalt, and a TES-
1330 based search for smectite clay minerals on Mars. Geophysical Research
1331 Letters, 34, L10204.

1332 Sapers, H.M., Razzell Hollis, J., Bhartia, R., Beegle, L.W., Orphan, V.J., and Amend, J.P.
1333 (2019) The Cell and the Sum of Its Parts: Patterns of Complexity in
1334 Biosignatures as Revealed by Deep UV Raman Spectroscopy. Frontiers in
1335 Microbiology, 10.

1336 [18]Schmidt, E.R., and Heystek, H. (1953) A saponite from Krugersdorp district,
1337 Transvaal. Mineralogical Magazine and Journal of the Mineralogical Society,
1338 30, 201-210.

1339 Schopf, J.W., Kudryavtsev, A.B., Agresti, D.G., Czaja, A.D., and Wdowiak, T.J. (2005)
1340 Raman Imagery: A New Approach to Assess the Geochemical Maturity and
1341 Biogenicity of Permineralized Precambrian Fossils. Astrobiology, 5, 333–371.

1342 Sholes, S.F., Smith, M.L., Claire, M.W., Zahnle, K.J., and Catling, D.C. (2017) Anoxic
1343 atmospheres on Mars driven by volcanism: Implications for past
1344 environments and life. Icarus, 290, 46–62.

1345 Socrates, G. (2004) Infrared and Raman Characteristic Group Frequencies: Tables
1346 and Charts, 390 p. John Wiley & Sons.

1347 [19] Son, B.-K., Yoshimura, T., and Fukasawa, H. (2001) Diagenesis of dioctahedral
1348 and trioctahedral smectites from alternating beds in Miocene to Pleistocene
1349 rocks of the Niigata Basin, Japan. Clays and Clay Minerals, 49, 333-346.

1350 [20] Suquet, H., Calle, C.D.L., and Pezerat, H. (1975) Swelling and structural
1351 organization of saponite. Clays and Clay Minerals, 23, 1-9.

1352 Tarafder, P.K., and Thakur, R. (2013) An Optimised 1,10-Phenanthroline Method for
1353 the Determination of Ferrous and Ferric Oxides in Silicate Rocks, Soils and
1354 Minerals. Geostandards and Geoanalytical Research, 37, 155–168.

1355 [21]Treiman, A.H., Morris, R.V., Agresti, D.G., Graff, T.G., Achilles, C.N., Rampe, E.B.,
1356 Bristow, T.F., Blake, D.F., Vaniman, D.T., Bish, D.L., and others (2014) Ferrian
1357 saponite from the Santa Monica Mountains (California, U.S.A., Earth):
1358 Characterization as an analog for clay minerals on Mars with application to
1359 Yellowknife Bay in Gale Crater. American Mineralogist, 99, 2234–2250.

1360 Uckert, K., Bhartia, R., and Michel, J. (2019) A Semi-Autonomous Method to Detect
1361 Cosmic Rays in Raman Hyperspectral Data Sets. Applied Spectroscopy, 73,
1362 1019–1027.

1363 Ufer, K., Roth, G., Kleeberg, R., Stanjek, H., Dohrmann, R., and Bergmann, J. (2004)
1364 Description of X-ray powder pattern of turbostratically disordered layer
1365 structures with a Rietveld compatible approach. Zeitschrift für
1366 Kristallographie - Crystalline Materials, 219, 519–527.

1367 Ulery, A.L., and Drees, L.R. (2008) Methods of soil analysis: Mineralogical methods.
1368 Part 5 Vol. 9. ASA-CSSA-SSSA.

1369 Vaniman, D.T., Bish, D.L., Ming, D.W., Bristow, T.F., Morris, R.V., Blake, D.F., Chipera,
1370 S.J., Morrison, S.M., Treiman, A.H., Rampe, E.B., and others (2013) Mineralogy
1371 of a Mudstone at Yellowknife Bay, Gale Crater, Mars. Science, 1243480.

1372 [22] Van Olphen, H., and Fripiat, J.J. (1979) Data Handbook for Clay Materials and
1373 Other Non-metallic Minerals. Pergamon Press, Oxford.

1374 [23] Vantelon, D., Montarges-Pelletier, E., Michot, L.J., Briois, V., Pelletier, M., and
1375 Thomas, F. (2003) Iron distribution in the octahedral sheet of dioctahedral
1376 smectites: An Fe K-edge X-ray absorption spectroscopy study. Physics and
1377 Chemistry of Minerals, 30, 44-53.

1378 Wang, A., Freeman, J.J., and Jolliff, B.L. (2015) Understanding the Raman spectral
1379 features of phyllosilicates. Journal of Raman Spectroscopy, 46, 829–845.

[24] Weir, A.H., and Greene-Kelly, R. (1962) Beidellite. American Mineralogist, 47, 137-146.

Wiens, R.C., Maurice, S., and Rull Perez, F. (2017) The SuperCam remote sensing instrument suite for the Mars 2020 rover mission: A preview. Spectroscopy, 32.

Tables

Table 1. Calculated molecular formulas of synthetic intermediate smectite samples.

Sample	Calculated Formula	Octahedral Occupancy	%Fe(II)[a]
A	$Ca_{0.37}Na_{0.10}[Fe^{III}_{1.68}Mg_{0.40}][Si_{3.32}Al_{0.51}Fe^{III}_{0.17}]O_{10}(OH)_2$	2.08	-
B	$Ca_{0.28}[Fe^{III}_{1.54}Mg_{0.64}][Si_{3.55}Al_{0.39}Fe^{III}_{0.06}]O_{10}(OH)_2$	2.18	-
C	$Ca_{0.35}Na_{0.22}[Fe^{III}_{1.24}Mg_{0.37}Al_{0.39}][Si_{3.43}Al_{0.57}]O_{10}(OH)_2$	2.00	-
D	$Ca_{0.35}Na_{0.23}[Fe^{III}_{1.04}Mg_{0.46}Al_{0.53}][Si_{3.44}Al_{0.56}]O_{10}(OH)_2$	2.03	-
E	$Ca_{0.40}[Fe^{III}_{1.06}Mg_{0.93}Al_{0.15}][Si_{3.70}Al_{0.30}]O_{10}(OH)_2$	2.14	-
F	$Ca_{0.35}Na_{0.07}[Fe^{III}_{0.96}Mg_{0.84}Al_{0.29}][Si_{3.80}Al_{0.20}]O_{10}(OH)_2$	2.09	-
G	$Ca_{0.24}[Fe^{III}_{0.69}Mg_{1.12}Al_{0.52}][Si_{3.66}Al_{0.34}]O_{10}(OH)_2$	2.33	-
H	$Ca_{0.39}[Fe^{III}_{0.68}Mg_{1.75}Al_{0.02}][Si_{3.60}Al_{0.40}]O_{10}(OH)_2$	2.45	-
I	$Ca_{0.31}Na_{0.28}[Fe^{III}_{0.57}Mg_{0.92}Al_{0.63}][Si_{3.67}Al_{0.33}]O_{10}(OH)_2$	2.12	-

J	$Ca_{0.37}[Fe^{III}_{0.27}Mg_{2.31}Al_{0.08}][Si_{3.60}Al_{0.40}]O_{10}(OH)_2$	2.66	-
K	$Ca_{0.23}[Fe^{II}_{2.23}Fe^{III}_{0.28}Al_{0.26}Mg_{0.12}][Si_{3.51}Al_{0.49}]O_{10}(OH)_2$	2.89	89.0
L	$Ca_{0.30}[Fe^{II}_{1.43}Fe^{III}_{0.23}Al_{0.40}Mg_{0.66}][Si_{3.55}Al_{0.45}]O_{10}(OH)_2$	2.72	86.0
M	$Ca_{0.29}Na_{0.05}[Fe^{II}_{1.50}Fe^{III}_{0.11}Al_{0.29}Mg_{0.92}][Si_{3.46}Al_{0.54}]O_{10}(OH)_2$	2.81	93.1
N	$Ca_{0.27}Na_{0.08}[Fe^{II}_{0.80}Fe^{III}_{0.09}Al_{1.29}Mg_{0.10}][Si_{3.54}Al_{0.46}]O_{10}(OH)_2$	2.28	90.0
O	$Ca_{0.28}Na_{0.12}[Fe^{II}_{0.64}Fe^{III}_{0.11}Al_{1.08}Mg_{0.50}][Si_{3.56}Al_{0.44}]O_{10}(OH)_2$	2.34	85.4
P	$Ca_{0.29}Na_{0.06}[Fe^{II}_{0.69}Fe^{III}_{0.11}Al_{0.35}Mg_{1.57}][Si_{3.57}Al_{0.43}]O_{10}(OH)_2$	2.72	86.6

[a] Mol.% of total iron occurring as Fe(II); only measured for syntheses involving iron(II) chloride.

Table 2. Measured peak positions of diagnostic diffraction features of the synthetic smectites using Cu K_α and their calculated corresponding positions for measurements using Co K_α radiation.

Sample	°2θ Cu Kα			°2θ Co Kα		
	(001)	(02,11)	(06,33)	(001)	(02,11)	(06,33)
A	6.00(8)[a]	19.61(1)	60.856(8)	6.97	22.81	72.04
B	6.29(2)	19.71(1)	60.93(1)	7.30	22.93	72.14
C	5.99(8)	19.63(1)	60.800(9)	6.96	22.83	71.97
D	6.31(3)	19.64(1)	60.87(1)	7.33	22.84	72.06
E	6.04(6)	19.76(2)	60.843(8)	7.01	22.98	72.02
F	6.06(4)	19.71(1)	60.806(8)	7.04	22.93	71.98
G	6.10(1)	19.68(1)	60.86(2)	7.08	22.89	72.05
H	6.13(1)	19.63(1)	60.718(6)	7.12	22.83	71.87
I	6.51(2)	19.72(1)	60.807(9)	7.56	22.94	71.98
J	6.37(2)	19.50(1)	60.584(4)	7.40	22.68	71.70

K	5.36(5)	19.21(3)	59.37(2) [b]	6.22	22.35	70.20
L	5.2(1)	19.28(1)	60.019(8)	6.10	22.42	71.00
M	5.46(6)	19.32(2)	60.096(7)	6.34	22.47	71.10
N	5.7(1)	19.89(1)	61.13(4) [b]	6.63	23.13	72.38
O	5.6(1)	19.81(2)	60.84(3) [b]	6.51	23.04	72.01
P	5.7(9)	19.50(2)	60.42(1)	6.62	22.68	71.51

[a] Numbers in parentheses represent fitting uncertainties in the last digit.
b Peaks consist of doublets but fitted as single feature. When modeled as doublets, contain peaks at 58.32(14)° and 59.61(5)° for K, 60.42(12)° and 61.86(10)° for N, and 60.29(12)° and 61.65(18)° for O.

Table 3. Comparison between d-spacings as derived from the fitted lattice parameters and as calculated from observed peak positions.

Sample	$d_{(001)}$ (Å)		$d_{(02,11)}$ (Å)		$d_{(06,33)}$ (Å)	
	Lattice	Peak	Lattice	Peak	Lattice	Peak
A	14.9	14.7	4.57	4.53	1.526	1.522
B	14.2	14.0	4.55	4.50	1.524	1.520
C	14.6	14.7	4.58	4.52	1.528	1.523
D	14.0	14.0	4.57	4.52	1.526	1.522
E	14.8	14.6	4.56	4.49	1.527	1.522
F	14.7	14.6	4.57	4.50	1.528	1.523
G	14.7	14.5	4.57	4.51	1.526	1.522
H	14.6	14.4	4.58	4.52	1.530	1.525
I	14.0	13.6	4.56	4.50	1.528	1.523
J	13.0	13.9	4.60	4.55	1.533	1.528
K	16.5	16.5	4.66	4.62	1.552	1.557 [a]
L	16.8	16.8	4.64	4.60	1.545	1.541
M	16.1	16.2	4.63	4.59	1.543	1.540

N	15.4	15.5	4.53	4.46	1.520	1.516 [a]
O	15.5	15.8	4.55	4.48	1.525	1.523 [a]
P	15.4	15.5	4.60	4.55	1.536	1.532

[a] Determined from position when fitting with a single peak. Fitting (06,33) bands as a double yield d-spacings of 1.582 Å and 1.551 Å for K, 1.532 Å and 1.500 Å for N, and 1.535 Å and 1.504 Å for O.

Table 4. Lattice parameters derived from refinement to individual peaks assuming hexagonal sheet symmetry.

Sample	**c (Å)**	**b (Å), (02,11)**	**b (Å), (06,33)**
A	14.87(12) [a]	9.146(7)	9.158(10)
B	14.18(3)	9.103(7)	9.147(11)
C	14.57(23)	9.150(8)	9.168(2)
D	14.04(18)	9.130(7)	9.154(5)
E	14.79(33)	9.122(7)	9.161(4)
F	14.72(21)	9.134(6)	9.167(5)
G	14.70(3)	9.135(3)	9.154(3)
H	14.61(19)	9.156(4)	9.179(2)
I	13.95(43)	9.126(9)	9.169(2)
J	13.02(16)	9.194(3)	9.197(2)
K	16.52(9)	9.329(4)	9.310(17)
L	16.80(12)	9.274(6)	9.268(3)
M	16.11(11)	9.252(10)	9.259(41)
N	15.39(10)	9.063(29)	9.119(15)

O	15.46(14)	9.102(13)	9.149(6)
P	15.35(12)	9.192(9)	9.217(2)

[a] Numbers in parentheses represent fitting uncertainties in the last digit.

Table 5. Isomer shift and quadrupole splitting of the Fe-rich smectite samples.

Smectite	Fe^{II} δ (mm s^{-1})	Fe^{II} ΔE_Q (mm s^{-1})	Fe^{III} δ (mm s^{-1})	Fe^{III} ΔE_Q (mm s^{-1})	Fe^{II}/Fe^{III}
A	--	--	0.35 ± 0.02	0.61 ± 0.01	0
B	--	--	0.35 ± 0.02	0.61 ± 0.01	0
C	--	--	0.36 ± 0.02	0.64 ± 0.01	0
D	--	--	0.36 ± 0.02	0.67 ± 0.01	0
E	--	--	0.34 ± 0.02	0.59 ± 0.01	0
F	--	--	0.35 ± 0.02	0.60 ± 0.01	0
K	1.11 ± 0.02	2.53 ± 0.01	0.40± 0 .02	0.77 ± 0.01	77.2
L	1.13 ± 0.02	2.59 ± 0.01	0.42 ± 0.02	0.61 ± 0.01	72.1
M	1.16 ± 0.02	2.54 ± 0.01	0.44 ± 0.02	0.58 ± 0.01	91.8

N	1.13 ± 0.02	2.63 ± 0.01	0.40 ± 0.02	0.55 ± 0.01	85.1
O	1.13 ± 0.02	2.61 ± 0.01	0.39 ± 0.02	0.55 ± 0.01	88.8

Table 6. Variation in the isomer shift in samples A and K as temperature is adjusted.

Temperature (K)	**δ (mm s^{-1}) – Sample A**	**δ (mm s^{-1}) – Sample K**
80	0.46 ± 0.01	1.26 ± 0.01
120	0.44 ± 0.01	1.24 ± 0.01
160	0.43 ± 0.01	1.22 ± 0.01
200	0.41 ± 0.01	-
240	0.39 ± 0.01	-
280	0.37 ± 0.01	-
293	0.35 ± 0.01	-
310	0.35 ± 0.01	1.15 ± 0.01
320	0.33 ± 0.01	1.13 ± 0.01

Figure Captions

Figure 1: Terrestrial continental and marine smectite clay minerals span a wide range of bulk compositions [references 1-24]. Common smectite spectral standard samples are highlighted as open circles; Fe in these standards is predominantly in the 3+ oxidation state.

Figure 2. Ternary diagrams showing the compositions of 16 synthetic ferruginous smectite samples investigated in this study. The full structural composition is shown

in the left diagram, whereas the right diagram shows the composition of the octahedral sheet only. Fe(III)-bearing samples are shown in brown circles. Fe(II)-bearing samples are shown in blue-green diamonds. Colors trend from light to dark with increasing octahedral Fe content. Colors are kept consistent in following figures. Small squares show the compositions of Clay Mineral society standards NAu-1, NAu-2, Ng-1, SWa-1, Sap-Ca1, SWy-1, SAz-1, STx-1b, SCa-3, SBId-1 that are frequently used as spectroscopic standards (Van Olphen et al., 1979, Post, 1984, Gates 2005, Gailhanou et al., 2012, Castellina et al., 2017).

Figure 3. (a) XRD patterns of the synthetic smectite samples. No background subtraction is performed to avoid aliasing broad features. (b) Peak positions of the (02,11) peaks and (c) of the 060 peak shift to smaller angles with decreasing Fe(III) content. (d) The calculated b-axis spacing based on fitting the (02, 11) peak with respect to octahedral occupancy; vertical lines delineate approximate distinctions between di, di-tri, and tri-octahedral structures. (e) Dioctahedral samples show little dependence of the d-spacing on octahedral iron content, although the trioctahedral Fe(II)-bearing samples show a more linear trend (trend lines fit only to the dioctahedral and trioctahedral samples, respectively).

Figure 4. Visible to near infrared reflectance spectra of (a) Fe(III) bearing smectite samples and (b) Fe(II) bearing smectite samples. (c) Continuum removed absorption features between 2.1 and 2.5 μm for all samples with wavelengths of

1559 overtones and combination absorptions from the literature indicated as detailed in
1560 the text.
1561
1562 Figure 5. Trends in the position and intensity of metal-OH combination absorptions.
1563 Larger data points indicate greater relative band depth of the absorption, from 0.01-
1564 0.34, and are relative across panels. a) Position of ~2.24μm absorptions as a
1565 function of octahedral magnesium. Absorptions at shorter wavelengths (~2.235μm)
1566 are attributed to Al-Mg-OH combination bands, whereas absorptions at longer
1567 wavelengths (~2.25μm) are attributed to Al-Fe(II)-OH combination bands. The
1568 samples with the highest Fe(III) content have low Al content and therefore have
1569 negligible Al-M-OH absorptions. Trend line is fit to both Fe(II) and Fe(III) bearing
1570 samples that have a measurable absorption. b) Position of the ~2.3 μm absorption
1571 as a function of octahedral Fe content. $Fe(II)_2$-OH combination modes trend towards
1572 2.36μm whereas $Fe(III)_2$-OH combination modes trend towards 2.29 μm. Mg-M-OH
1573 combinations trend towards 2.31 μm. c) Position of the ~2.45μm absorption as a
1574 function of octahedral Mg content. This feature is broad and shallow in the Fe(III)-
1575 bearing samples, without a significant trend, but the Fe(II)-bearing samples
1576 demonstrate a linear trend towards shorter wavelengths with increasing octahedral
1577 Mg content.
1578
1579 Figure 6. Attenuated Total Reflectance (ATR) spectra of the synthetic ferruginous
1580 smectite suite. (a) The hydroxyl bending modes and (b) the hydroxyl and

tetrahedral stretching modes. Peak attributions are described in the text. The peak at ~850cm^{-1} in the shaded box is attributed to calcite contamination in sample P.

Figure 7. (a) Mid-infrared Diffuse Reflectance spectra of the M-OH stretching modes of the sample suite. The deep broad feature around 3μm is caused by the fundamental H_2O stretching mode, and the narrower absorptions superimposed are the M-OH absorptions. (b) The position of the M-OH absorption as a function of octahedral iron content. The minima of both sample sets shifts to longer wavelengths with increasing octahedral iron, but the Fe(II) and Fe(III) bearings samples are offset from each other.

Figure 8: (a) Mid-infrared Diffuse Reflectance spectra of the silicate bending and stretching and M-OH bending modes, scaled and offset to emphasize features. A peak attributed to calcite contamination in sample P is indicated by the translucent box. Other peak attributions are discussed in the text. (b) The position of the Si-O bend between 430-480cm^{-1} is dependent on octahedral Fe content, with decreasing iron shifting the peak position to longer wavenumbers. Fe(II) bearing samples are offset to longer wavenumbers than Fe(III)-bearing samples. (c)The Fe(III) samples show a $Fe(III)_2$-OH bending mode around 845 cm^{-1} that shifts in position as a function of octahedral iron. M-OH bending modes are much more subdued in the Fe(II) samples, although the Fe-OH and Mg-OH bends around 650 cm^{-1} are apparent in all samples. (d) The position of the Si-O stretch does not shift as a function of composition in the Fe(III)-bearing samples, but increasing Al content in the Fe(II)-

1604 bearings samples does shift this mode to larger wavenumbers. The trend line is only
1605 fit to the Fe(II) samples.
1606
1607 Figure 9. (a)Raman patterns obtained using a 532nm excitation laser. (b) Raman
1608 shifts between 100-1200 cm^{-1} highlight silicate stretching and bending modes and
1609 overlapping metal-OH bends. (c) Metal-OH stretching modes occur between 3000-
1610 4000cm^{-1}. Labeled features are discussed in the text.
1611
1612 Figure 10: (a) Raman spectra obtained using a 248.6 nm excitation laser from 700-
1613 4000cm^{-1}, and (b) the M-OH stretching region from 3000-4000cm^{-1}. (c) The Si-O
1614 stretching mode is detected around 1060cm^{-1} and (d) the normalized signal
1615 intensity decreases as Fe content increases, due to increased UV absorption. (e) The
1616 peak and shoulder positions of the Fe(II), Fe(III), Al and Mg-OH stretching modes
1617 shift as a function of composition.
1618

1619 Figure 11: Mössbauer spectra for (a) Fe(II)-bearing smectite samples A-F at room
1620 temperature and (b) of Fe(II)-bearing smectite samples K-O. The Isomer Shifts are
1621 shown as diamonds and the quadrupole splitting ΔE_Q is shown as circles for the (c)
1622 Fe(II)-bearing samples and (d) Fe(II)-bearing samples.

1623 Figure 12. The Isomer shift is temperature dependent. (a) Mössbauer spectra of 'A'
1624 collected from 80 to 320 K with 40 K intervals in black and the fit in red. The spectra
1625 are referenced to the centroid of the spectrum of a α-Fe foil at room temperature.

1626 (b) The isomer shift of A decreases as a function of increasing temperature. (c)
1627 Mössbauer spectra of sample K collected from 80 to 293 K. (d). The isomer shift of K
1628 decreases as temperature increases.

Figure 1

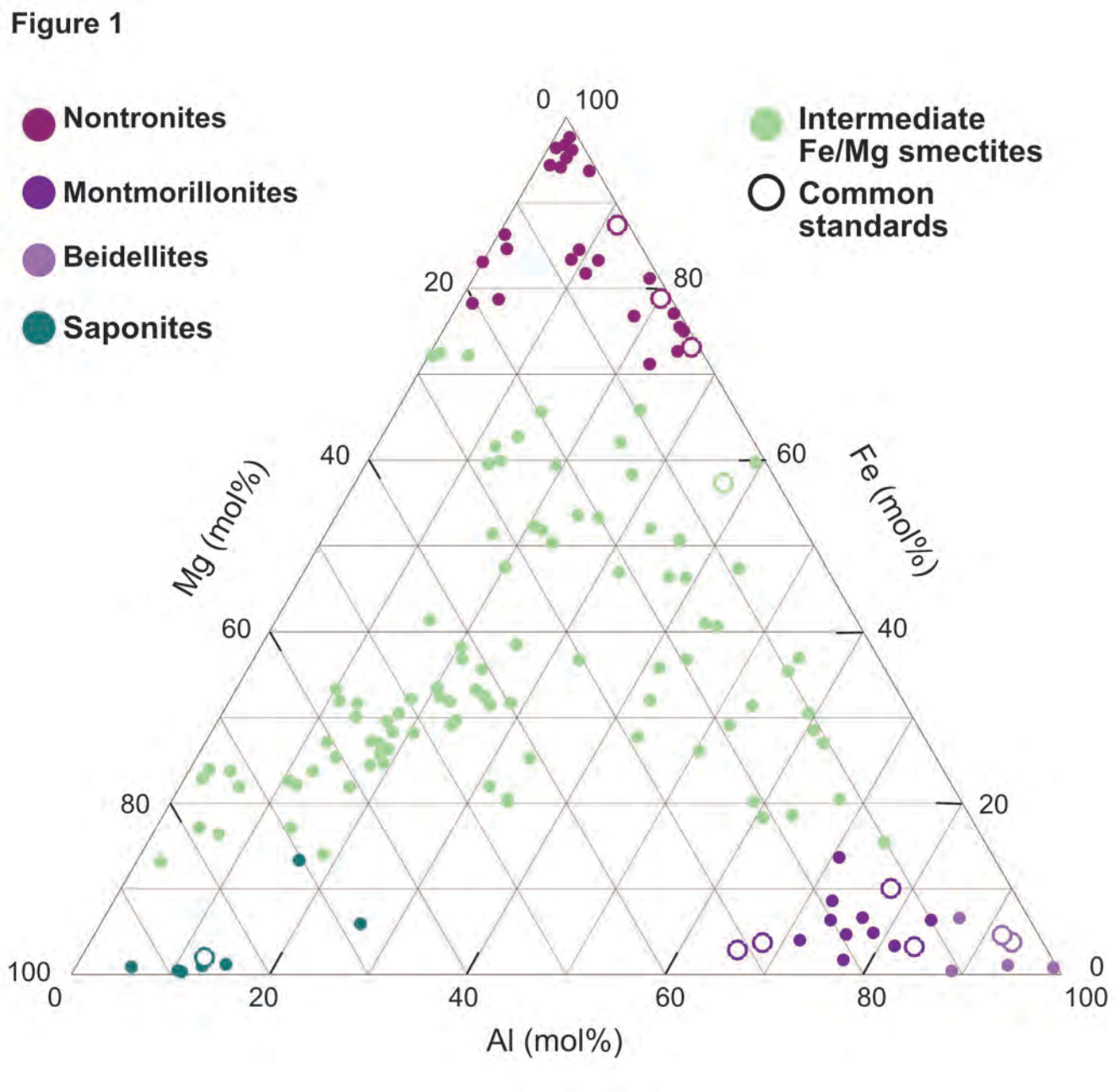
Nontronites
Montmorillonites
Beidellites
Saponites
Intermediate Fe/Mg smectites
Common standards
Mg (mol%)
Fe (mol%)
Al (mol%)
0
20
40
60
80
100

Figure 2

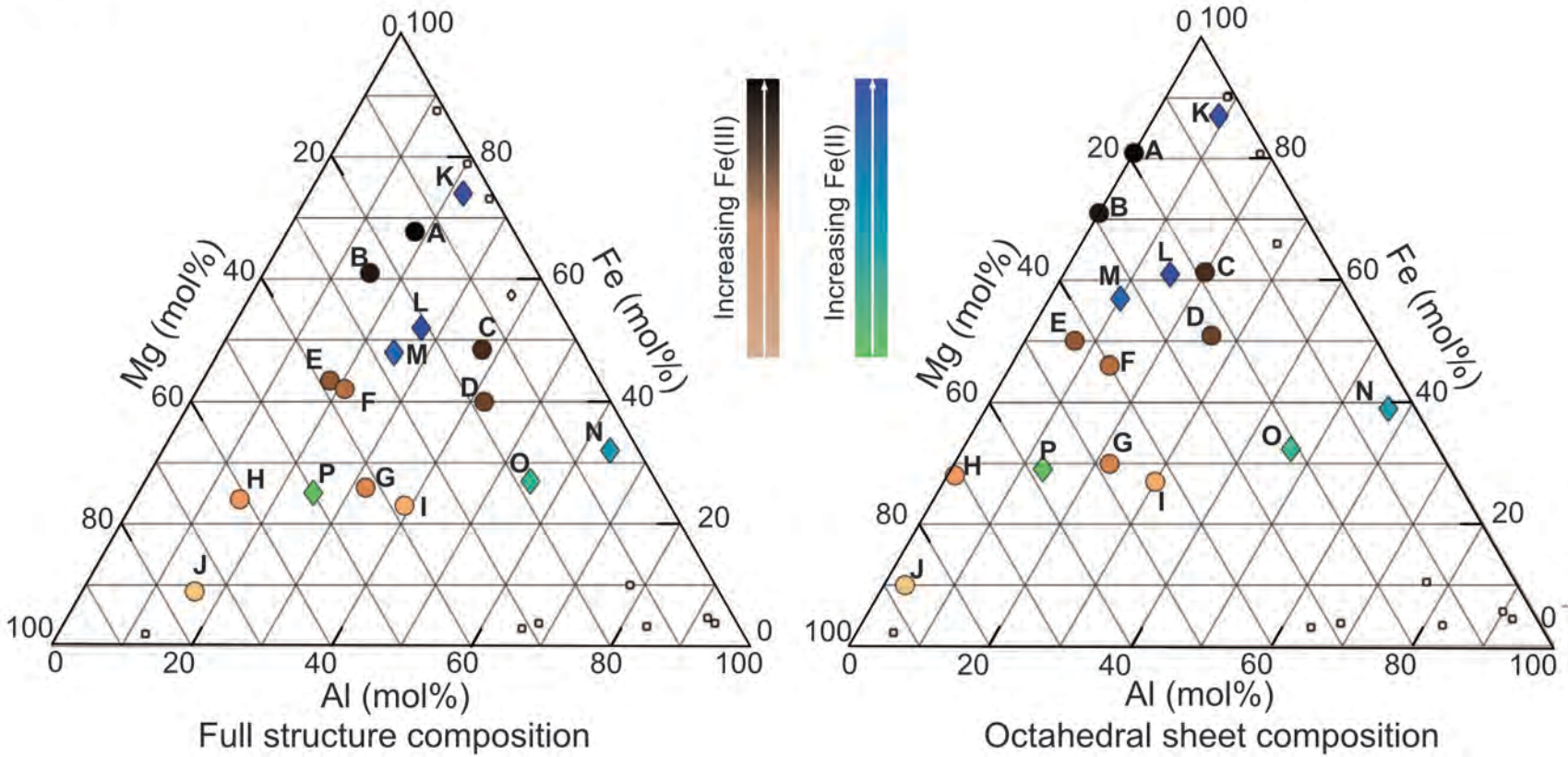
Mg (mol%)
Fe (mol%)
Al (mol%)
Increasing Fe(III)
Increasing Fe(II)
A
B
C
D
E
F
G
H
I
J
K
L
M
N
O
P
Full structure composition
Octahedral sheet composition

Figure 3.

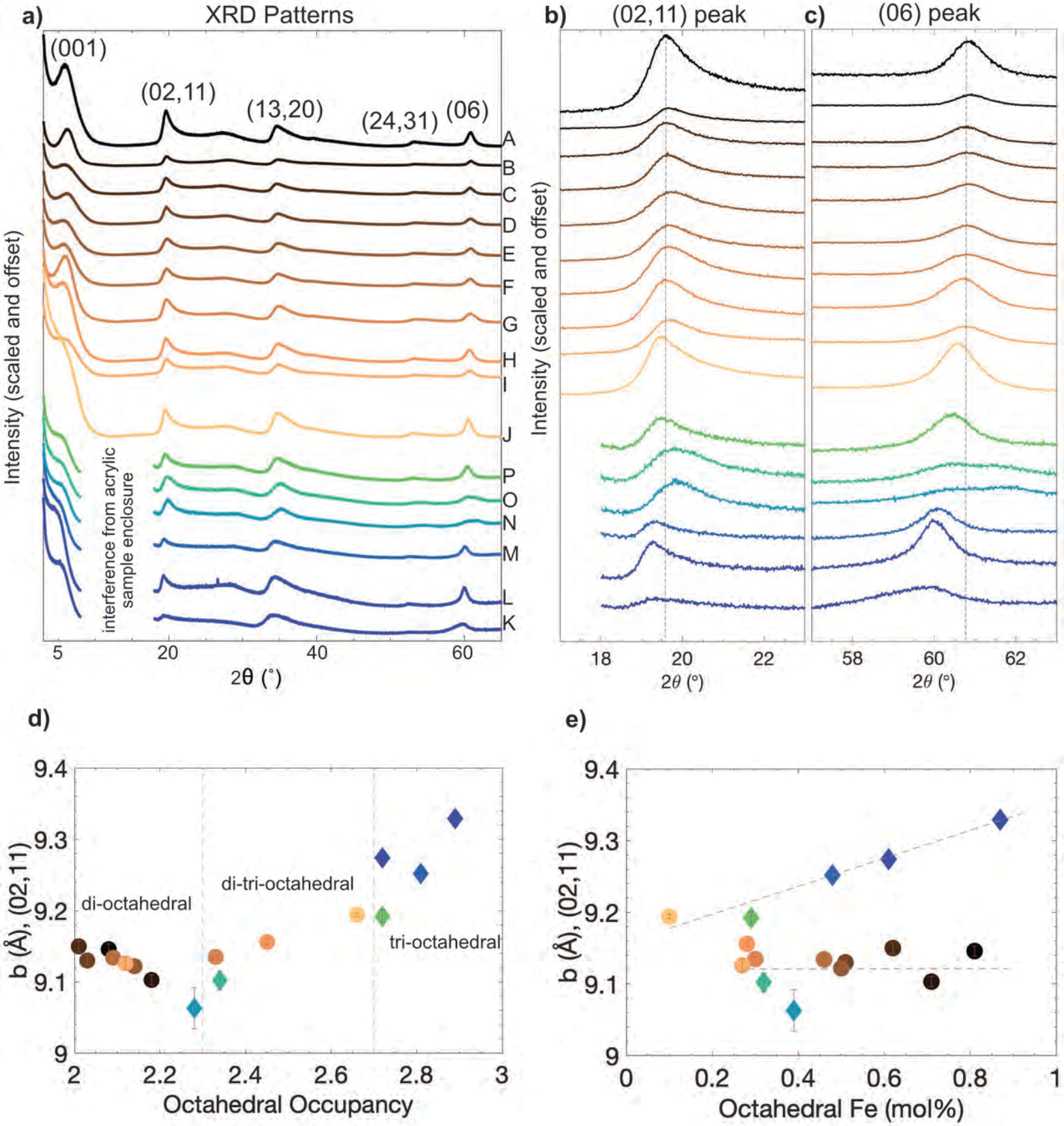
a)
XRD Patterns
(001)
(02,11)
(13,20)
(24,31)
(06)
A
B
C
D
E
F
G
H
I
J
P
O
N
M
L
K
interference from acrylic sample enclosure
Intensity (scaled and offset)
5
20
40
60
2θ (˚)
b)
(02,11) peak
c)
(06) peak
Intensity (scaled and offset)
18
20
22
2θ (°)
58
60
62
2θ (°)
d)
9.4
9.3
9.2
9.1
9
b (Å), (02,11)
di-octahedral
di-tri-octahedral
tri-octahedral
2
2.2
2.4
2.6
2.8
3
Octahedral Occupancy
e)
9.4
9.3
9.2
9.1
9
b (Å), (02,11)
0
0.2
0.4
0.6
0.8
1
Octahedral Fe (mol%)

Figure 4

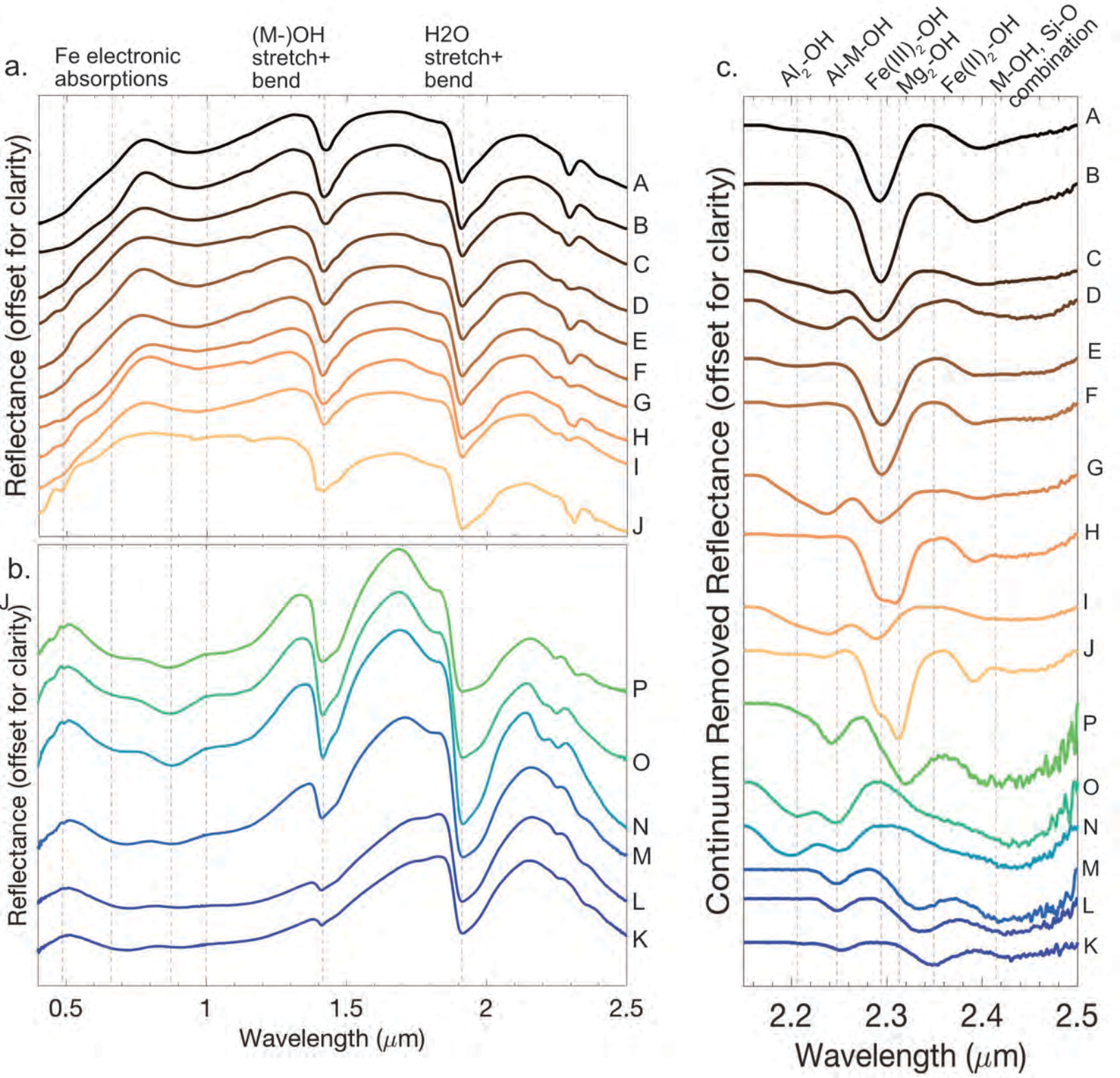
a.
Fe electronic absorptions
(M-)OH stretch+ bend
H2O stretch+ bend
Reflectance (offset for clarity)
A
B
C
D
E
F
G
H
I
J
b.
Reflectance (offset for clarity)
P
O
N
M
L
K
0.5
1
1.5
2
2.5
Wavelength (μm)
c.
Al2-OH
Al-M-OH
Fe(III)2-OH
Mg2-OH
Fe(II)2-OH
M-OH, Si-O combination
Continuum Removed Reflectance (offset for clarity)
A
B
C
D
E
F
G
H
I
J
P
O
N
M
L
K
2.2
2.3
2.4
2.5
Wavelength (μm)

Figure 5

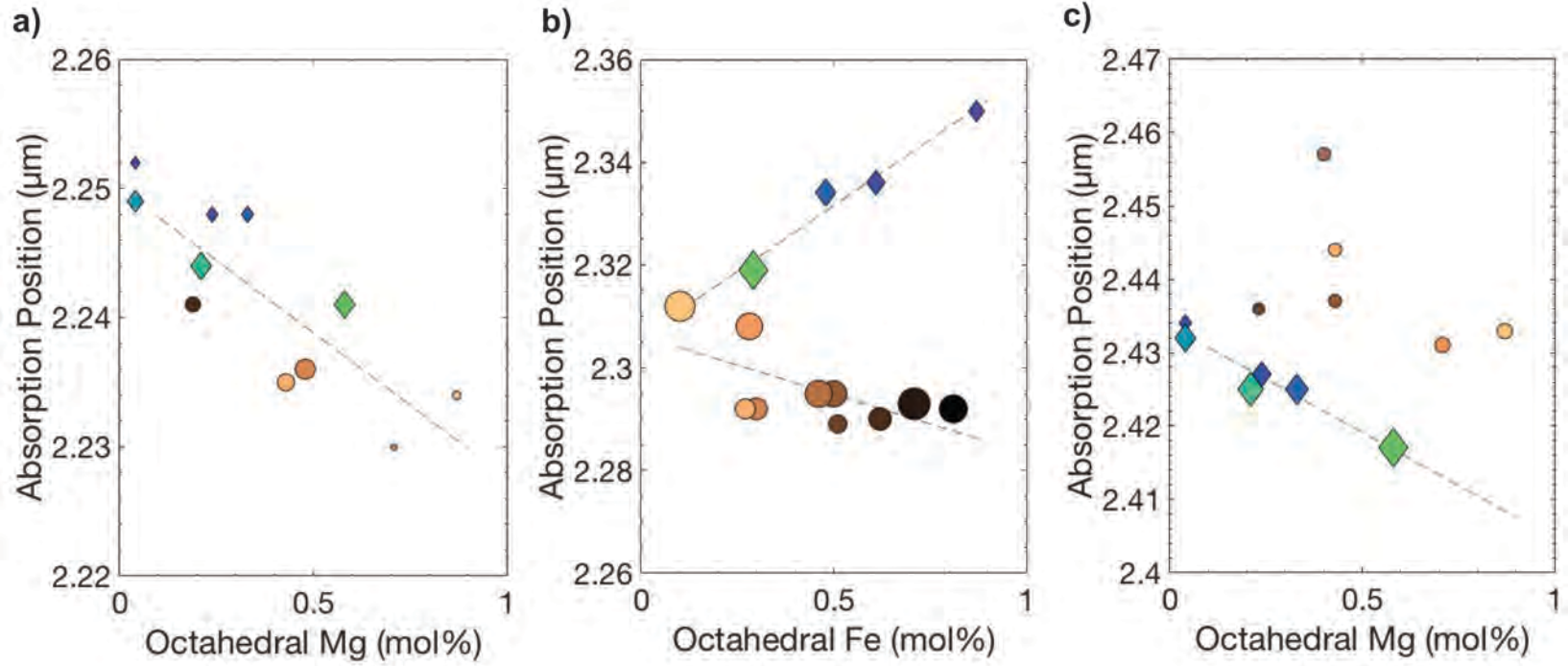
a)
b)
c)
Absorption Position (μm)
Octahedral Mg (mol%)
Octahedral Fe (mol%)
2.26
2.25
2.24
2.23
2.22
2.36
2.34
2.32
2.3
2.28
2.47
2.46
2.45
2.44
2.43
2.42
2.41
2.4
0
0.5
1

Figure 6

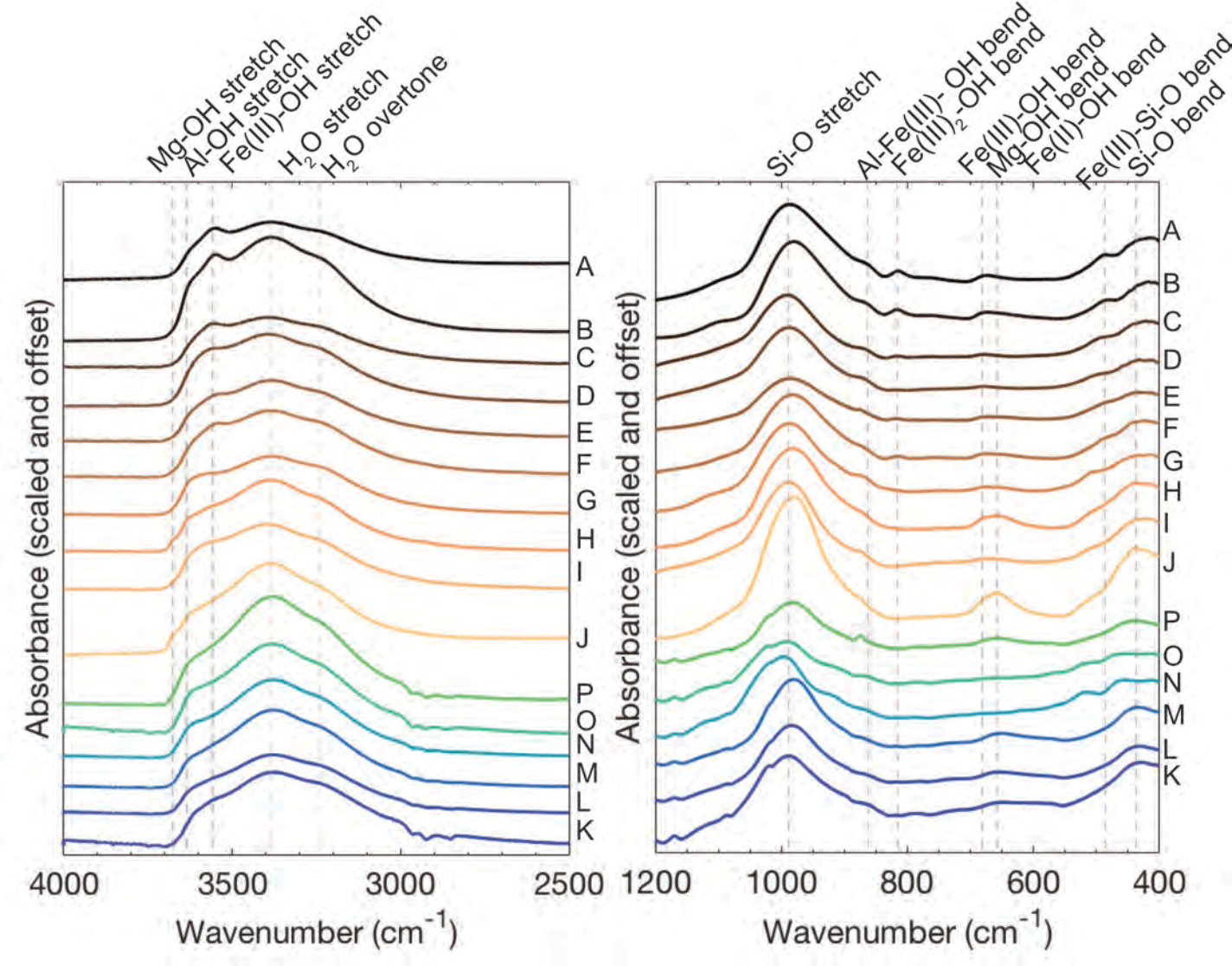
Mg-OH stretch
Al-OH stretch
Fe(III)-OH stretch
H_2O stretch
H_2O overtone
Absorbance (scaled and offset)
A
B
C
D
E
F
G
H
I
J
P
O
N
M
L
K
4000
3500
3000
2500
Wavenumber (cm^{-1})
Si-O stretch
Al-Fe(III)- OH bend
$Fe(III)_2$-OH bend
Fe(III)-OH bend
Mg-OH bend
Fe(II)-OH bend
Fe(III)-Si-O bend
Si-O bend
Absorbance (scaled and offset)
A
B
C
D
E
F
G
H
I
J
P
O
N
M
L
K
1200
1000
800
600
400
Wavenumber (cm^{-1})

Figure 7

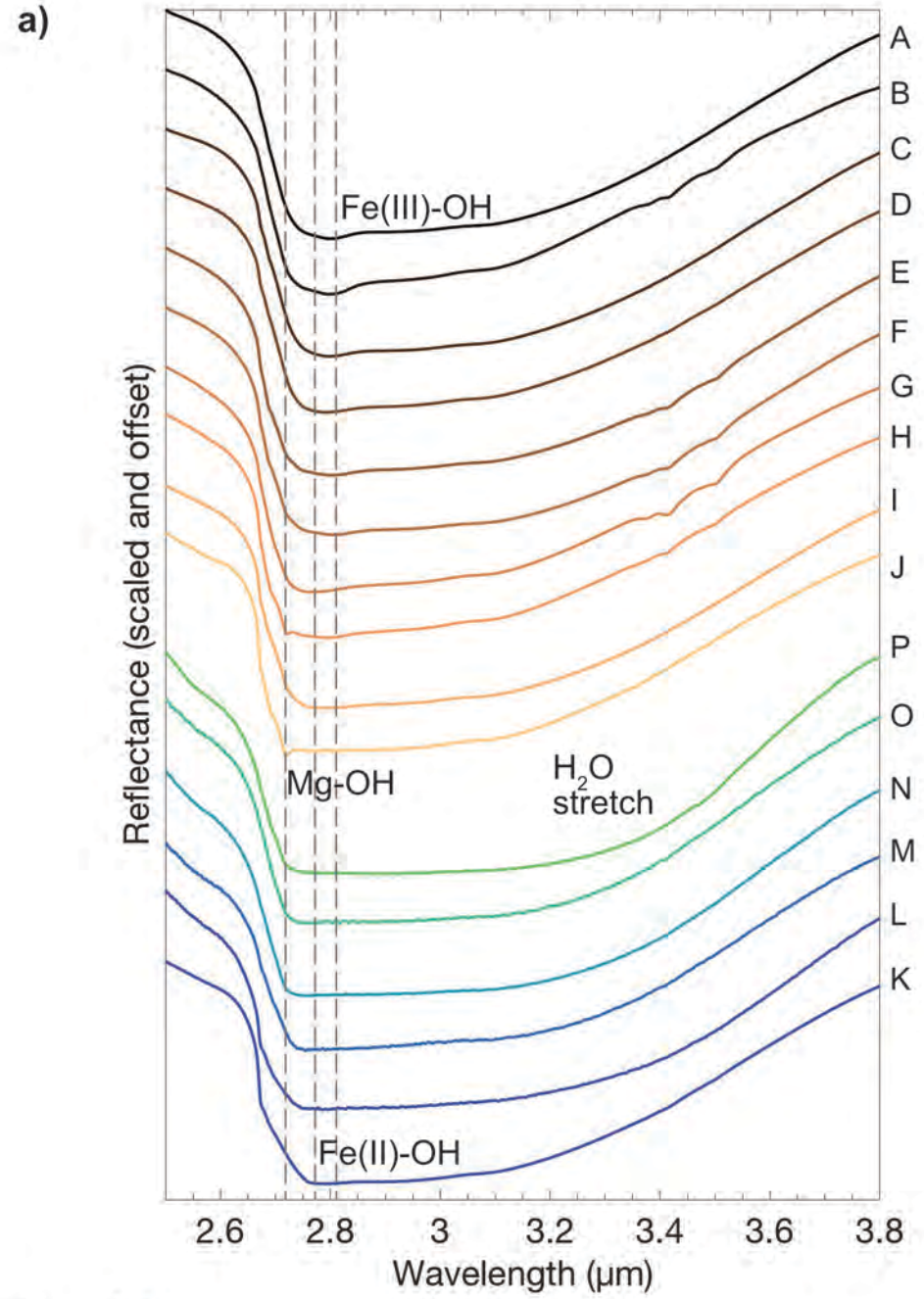
a)
A
B
C
D
E
F
G
H
I
J
P
O
N
M
L
K
Fe(III)-OH
Mg-OH
H2O stretch
Fe(II)-OH
Reflectance (scaled and offset)
2.6
2.8
3
3.2
3.4
3.6
3.8
Wavelength (μm)

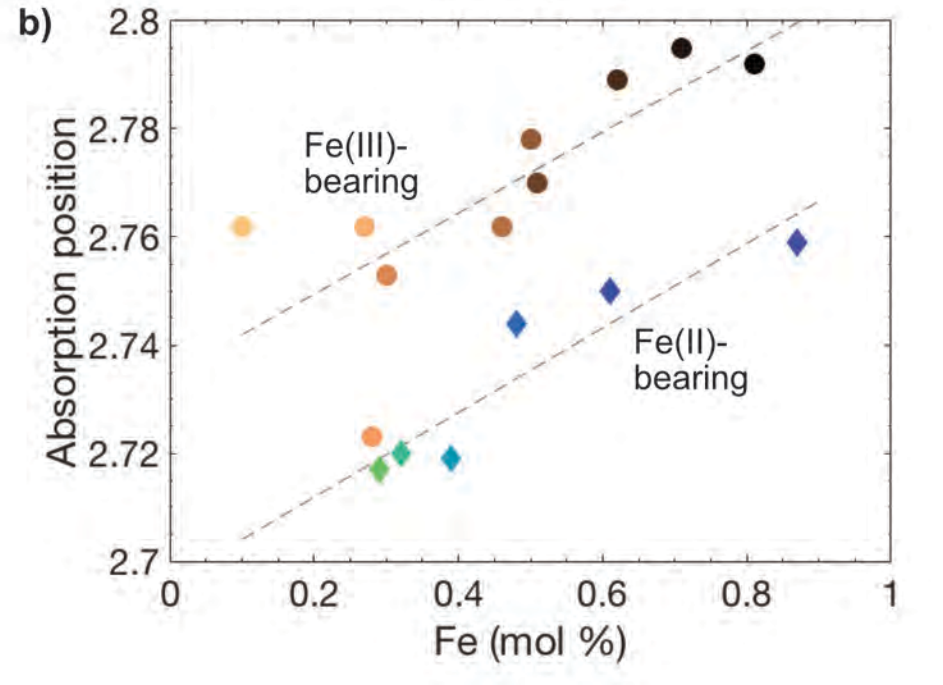
b)
2.8
2.78
2.76
2.74
2.72
2.7
Absorption position
Fe(III)-bearing
Fe(II)-bearing
0
0.2
0.4
0.6
0.8
1
Fe (mol %)

Figure 8

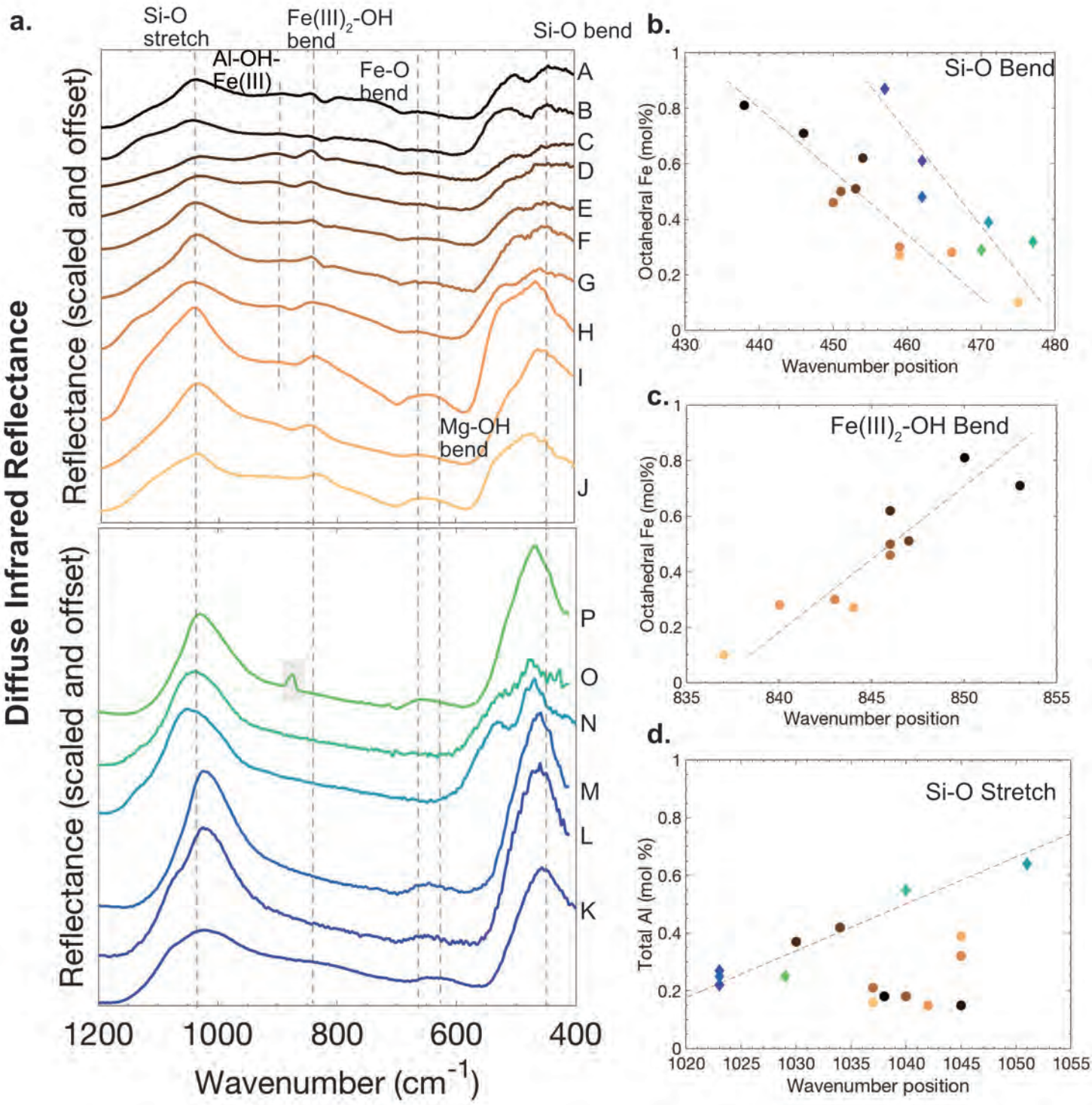
a.
Si-O stretch
Al-OH-Fe(III)
Fe(III)2-OH bend
Fe-O bend
Si-O bend
A
B
C
D
E
F
G
H
I
J
Mg-OH bend
Reflectance (scaled and offset)
P
O
N
M
L
K
Diffuse Infrared Reflectance
1200
1000
800
600
400
Wavenumber (cm-1)
b.
Si-O Bend
Octahedral Fe (mol%)
Wavenumber position
c.
Fe(III)2-OH Bend
Octahedral Fe (mol%)
Wavenumber position
d.
Si-O Stretch
Total Al (mol %)
Wavenumber position

Figure 9

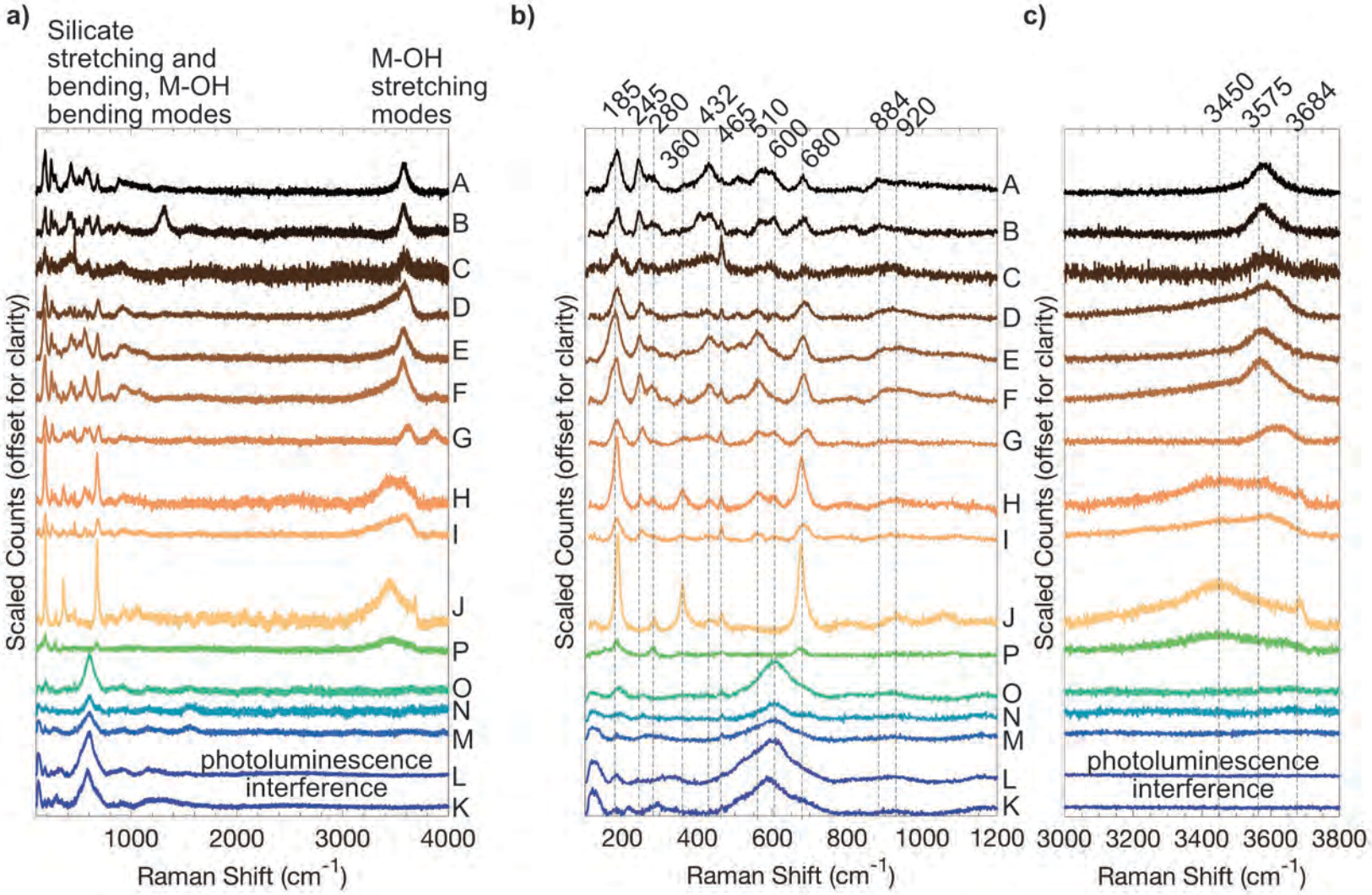
a)
Silicate stretching and bending, M-OH bending modes
M-OH stretching modes
Scaled Counts (offset for clarity)
A
B
C
D
E
F
G
H
I
J
P
O
N
M
photoluminescence
interference
L
K
1000
2000
3000
4000
Raman Shift (cm-1)
b)
185
245
280
360
432
465
510
600
680
884
920
Scaled Counts (offset for clarity)
200
400
600
800
1000
1200
Raman Shift (cm-1)
c)
3450
3575
3684
Scaled Counts (offset for clarity)
photoluminescence
interference
3000
3200
3400
3600
3800
Raman Shift (cm-1)

Figure 10

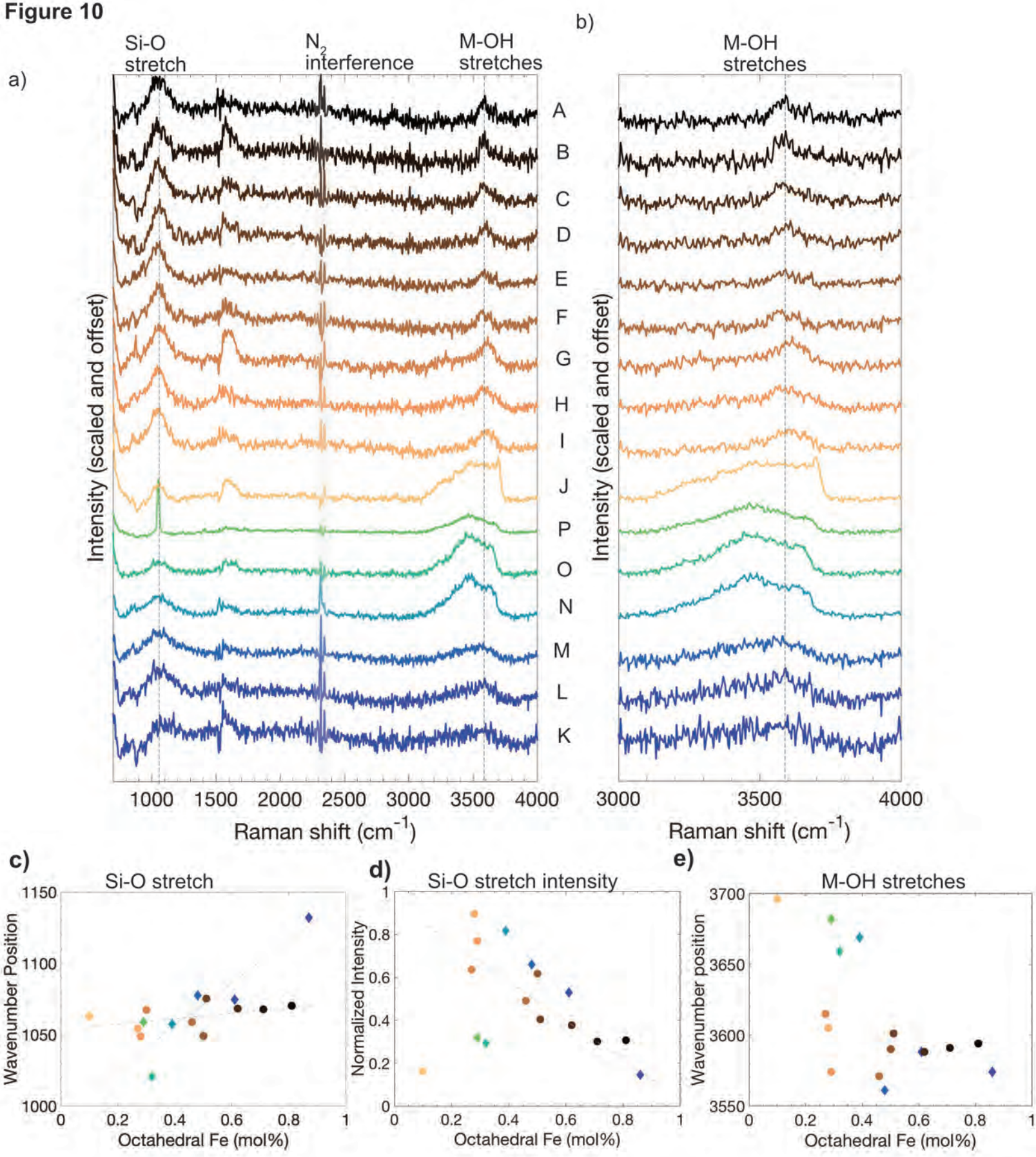
a)
Si-O stretch
N2 interference
M-OH stretches
A
B
C
D
E
F
G
H
I
J
P
O
N
M
L
K
Intensity (scaled and offset)
1000 1500 2000 2500 3000 3500 4000
Raman shift (cm-1)
b)
M-OH stretches
Intensity (scaled and offset)
3000 3500 4000
Raman shift (cm-1)
c)
Si-O stretch
Wavenumber Position
1150 1100 1050 1000
0 0.2 0.4 0.6 0.8 1
Octahedral Fe (mol%)
d)
Si-O stretch intensity
Normalized Intensity
1 0.8 0.6 0.4 0.2 0
0 0.2 0.4 0.6 0.8 1
Octahedral Fe (mol%)
e)
M-OH stretches
Wavenumber position
3700 3650 3600 3550
0 0.2 0.4 0.6 0.8 1
Octahedral Fe (mol%)

Figure 11

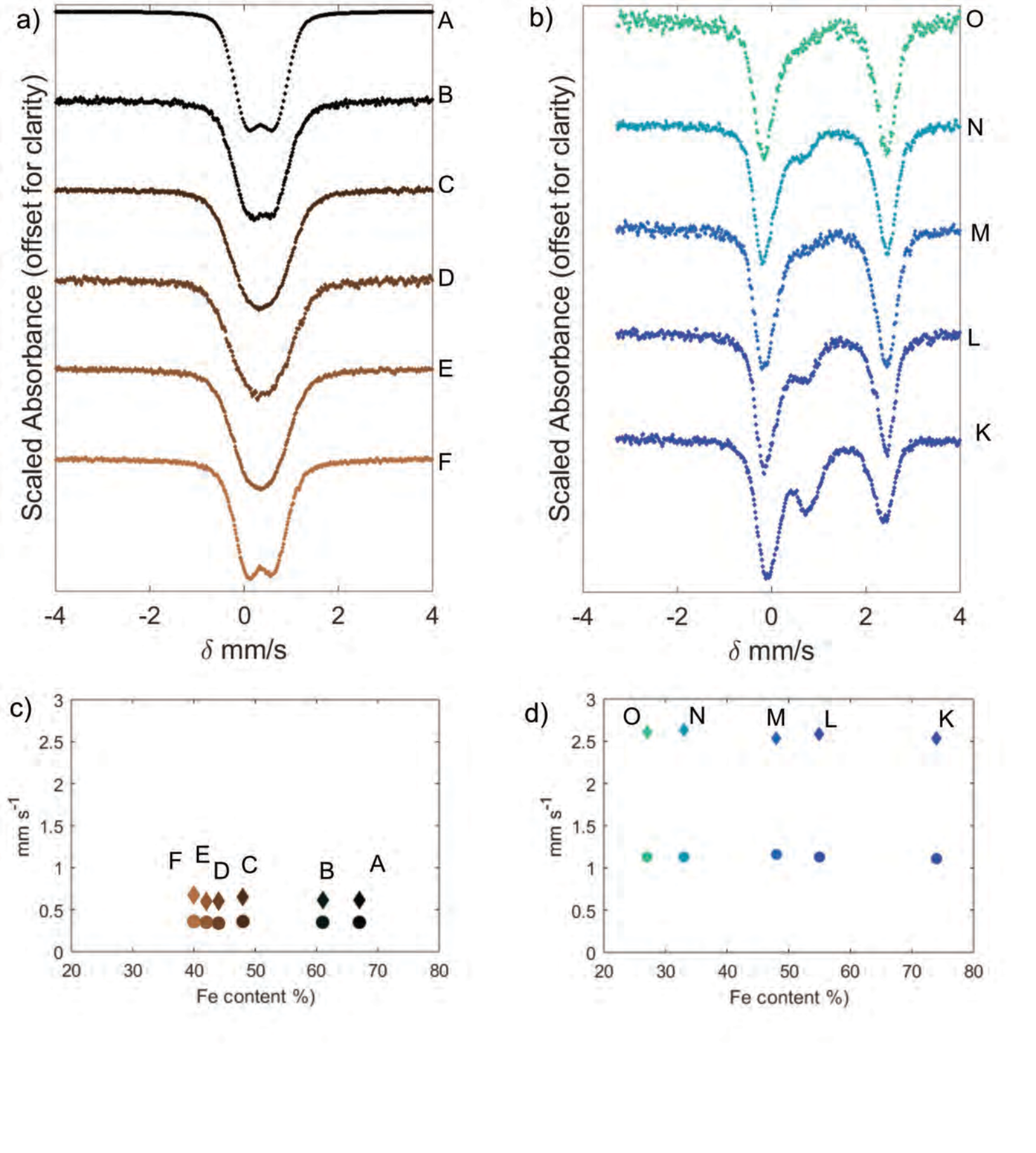
a)
A
B
C
D
E
F
Scaled Absorbance (offset for clarity)
-4
-2
0
2
4
δ mm/s
b)
O
N
M
L
K
Scaled Absorbance (offset for clarity)
-4
-2
0
2
4
δ mm/s
c)
mm s-1
0
0.5
1
1.5
2
2.5
3
F
E
D
C
B
A
20
30
40
50
60
70
80
Fe content %)
d)
mm s-1
0
0.5
1
1.5
2
2.5
3
O
N
M
L
K
20
30
40
50
60
70
80
Fe content %)

Figure 12

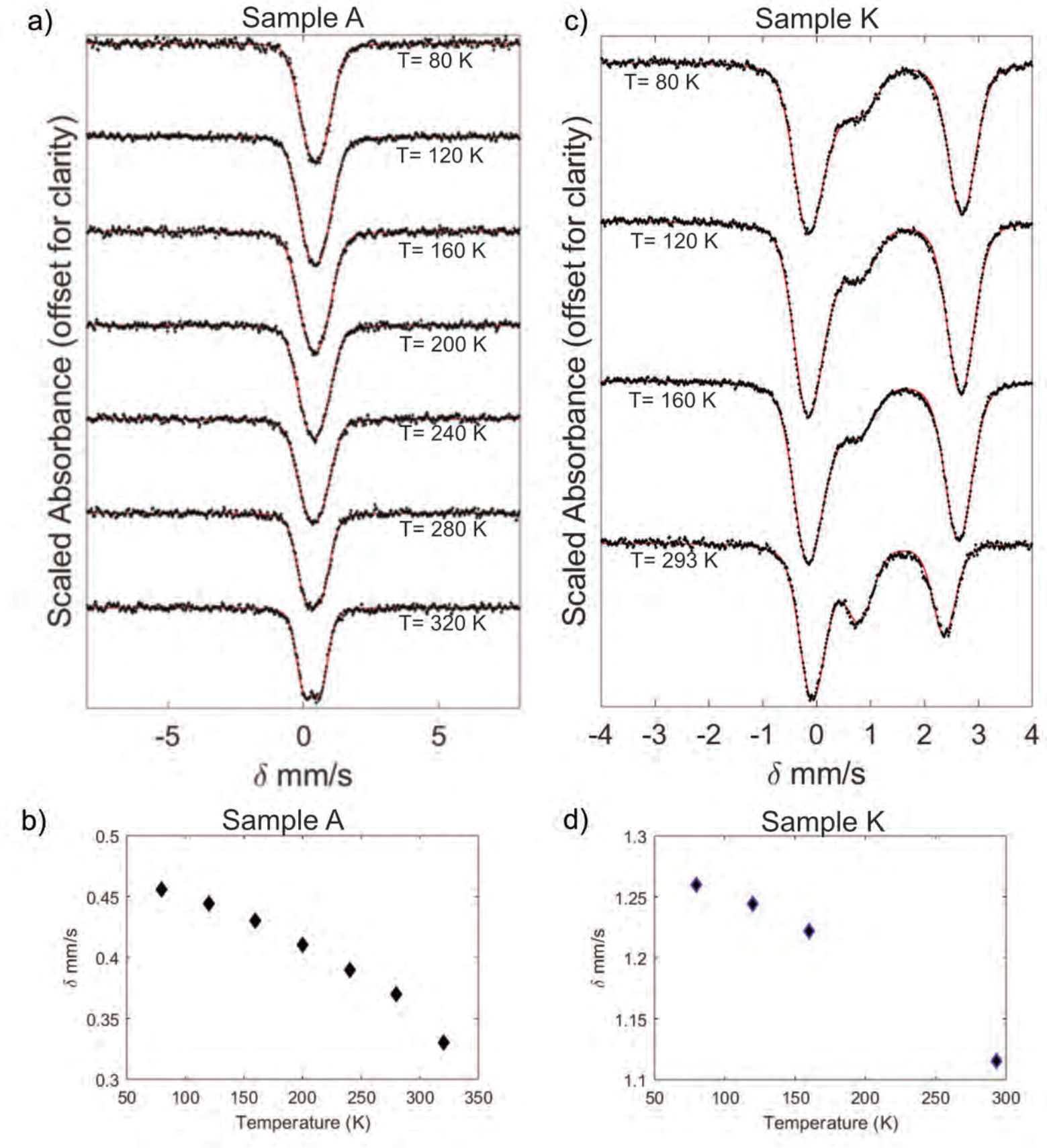
a)
Sample A
T= 80 K
T= 120 K
T= 160 K
T= 200 K
T= 240 K
T= 280 K
T= 320 K
Scaled Absorbance (offset for clarity)
-5
0
5
δ mm/s
c)
Sample K
T= 80 K
T= 120 K
T= 160 K
T= 293 K
Scaled Absorbance (offset for clarity)
-4
-3
-2
-1
0
1
2
3
4
δ mm/s
b)
Sample A
δ mm/s
0.5
0.45
0.4
0.35
0.3
50
100
150
200
250
300
350
Temperature (K)
d)
Sample K
δ mm/s
1.3
1.25
1.2
1.15
1.1
50
100
150
200
250
300
Temperature (K)